

The Cost of Circularity: Quantifying Eccentricity-Induced Biases in Binary Black Hole Inference

Tamal RoyChowdhury,¹ V. Gayathri,¹ Rossella Gamba,^{2,3}
Shubhagata Bhaumik,⁴ Imre Bartos,⁴ and Jolien Creighton¹

¹*Leonard E. Parker Center for Gravitation, Cosmology, and Astrophysics,
University of Wisconsin–Milwaukee, Milwaukee, WI 53201, USA*

²*Institute for Gravitation & the Cosmos, Department of Physics & Department of Astronomy and Astrophysics,
The Pennsylvania State University, University Park, Pennsylvania 16802, USA*

³*Department of Physics, University of California, Berkeley, CA 94720, USA*

⁴*Department of Physics, University of Florida, PO Box 118440, Gainesville, FL 32611-8440, USA*

(Dated: March 4, 2026)

Dynamically assembled binary black holes are expected to retain measurable orbital eccentricity in the LIGO-Virgo-KAGRA band, but most parameter estimation analyses still assume quasi-circular inspirals. This raises a critical question: how strongly does unmodeled eccentricity bias the inferred properties of BBH mergers? We address this by injecting eccentric signals generated with TEOBRESUMS-DALÍ and recovering them using the circular, precessing IMRPHENOMXPHM waveform model. Across 20-80 M_{\odot} and eccentricities up to $e = 0.5$, we find that circular waveform models remain reliable only for very small eccentricities. Above $e \sim 0.2$ at 10 Hz, recovered masses, spins, inclination, and distances begin to show significant systematic offsets. Circular precessing templates mimic eccentric amplitude and phase modulations by introducing artificial precession, highlighting a major degeneracy between these effects. For high-mass, moderately eccentric mergers, circular models misestimate parameters at a level that would bias astrophysical interpretation and population studies. Our results establish the parameter-space boundaries where eccentric waveform models become essential for accurate inference in current and next-generation detectors.

I. INTRODUCTION

The fourth observing run (O4) of Advanced LIGO [1], Advanced Virgo [2], and KAGRA [3] recently concluded, with analysis of the collected data ongoing. Prior to this, three observing runs were successfully completed, resulting in 91 confident detections of compact binary coalescences (CBCs) [4–8]. From the first part of the fourth observing run, named O4a, 128 new candidate events have been released, encompassing binaries with a wide range of masses and mass ratios, including previously unobserved types of binary systems [9]. Among these confirmed detections, we have detected two intermediate mass black hole binary systems, namely GW190521 [10] and GW231123 [7]. The event GW231123 was detected in the first half of the fourth observation run and has a total mass of about 190 – 265 M_{\odot} , making it the most massive binary black hole observed through GWs to date. We expect to see more of these types of extraordinary binaries in the current and future observing runs [11, 12].

The current parameter estimation (PE) analyses in the LIGO-Virgo-KAGRA (LVK) collaboration have significantly improved our understanding of the astrophysical properties of CBCs. The fourth observing run has yielded more precise measurements of component masses, spins, luminosity distances, and orbital orientations by incorporating advanced waveform models and Bayesian inference techniques [6, 8, 9]. They now allow exploration beyond the quasi-circular approximation. The improvements in waveforms have enabled the study of various subdominant effects such as orbital eccentricity, spin precession, and deviations from general relativity. Such extensions

are crucial for avoiding biases in parameter recovery. They also help to better constrain the astrophysical formation scenarios that are expected to produce compact binaries.

Dedicated eccentric binary black hole (eBBH) searches have been performed in the first, second, and third observing runs [13, 14]. These studies did not report any confident detections of binaries with non-negligible orbital eccentricity. This work assumes that all binaries have circular orbits and estimates their parameters accordingly [8]. Several studies have been conducted to estimate the orbital eccentricity of detected Binary Black Hole (BBH) systems [15, 16]. Notably, GW190521 has been identified as an eccentric binary based on results from analyses using different parameter estimation methods and waveform models [17–19]. Nonetheless, certain events show mild deviations from circularity, motivating the development and application of eccentric waveform families such as SEOBNRv5EHM [20, 21] and TEOBRESUMS-DALÍ [22–24] for inferring properties of such events. These waveform models facilitate a joint inference of masses, spins, and eccentricities. This allows us to distinguish between dynamical formation channels and isolated binary evolution, as a non-zero eccentricity is a direct confirmation that the event originated via the dynamical formation channel [25–27]. Accurate eccentricity estimation remains challenging due to waveform degeneracies and the need for high signal-to-noise ratios.

Eccentricity measurements have strong astrophysical significance because eccentric orbits are indicative of dynamical formation scenarios. Binaries formed through dynamical interactions in dense stellar environments,

such as globular clusters, galactic nuclei, active galactic nuclei (AGN), or hierarchical triples undergoing Kozai-Lidov oscillations, can retain measurable eccentricities in the LIGO band [28, 29]. The AGN formation channel, characterized by dense environments, can produce eccentric binaries through binary-single interactions [30]. In the case of binaries formed through isolated stellar evolution, they are expected to circularize due to gravitational-wave emission long before merger [31]. Thus, a reliable detection of eccentricity can serve as a crucial probe of the relative contributions of various formation channels.

Both eccentricity and spin precession introduce complex amplitude and phase modulations in the waveform [32, 33]. A notable challenge in such analyses is the degeneracy between eccentricity and precession. Certain precession-induced modulations in the waveform can mimic the features produced by moderate eccentricity, complicating their disentanglement, particularly for low-SNR events [34] and high mass ones [35]. Addressing this degeneracy requires the development of accurate waveform models that jointly incorporate both effects, as well as advanced statistical inference methods. A better understanding of these phenomena is key to improving the accuracy of parameter estimation and constraining the astrophysical origins of gravitational-wave sources.

Several studies have investigated how parameter-estimation pipelines behave when analyzing eccentric gravitational-wave signals using waveform models that assume quasi-circular orbits. Because circular templates cannot reproduce the characteristic modulation, higher harmonics, and phase evolution of eccentric binaries, it leads to systematic biases in the recovery of parameters. Simulation studies injecting eccentric signals and recovering them with circular waveform models ([36–40]) show that the inferred masses are typically biased toward lower mass ratios, spins are often misestimated – sometimes interpreted as artificial anti-alignment, and the luminosity distance is overestimated due to a loss in matched-filter efficiency. These analyses consistently find that even mild eccentricity ($e \geq 0.1$ at 10 Hz) produces noticeable deviations in the posteriors, while moderate eccentricity can cause the sampler to converge on incorrect modes altogether. Such studies highlight that quasi-circular models remain reasonably robust only for very low residual eccentricity, and they emphasize the need for eccentric waveform models in PE pipelines to avoid systematic errors in source characterization.

In this study, we investigate the systematic effects of orbital eccentricity on parameter estimation in the eBBH parameter space. We perform a series of equal mass non-spinning eccentric BBH injections across a range of masses and eccentricities, while keeping other parameters fixed, by using an eccentric waveform model. We use a quasi-circular waveform with spins for parameter recovery and do a qualitative study of the biases observed in the recovered parameters. We aim to find the parameter space in which the inclusion of eccentricity for parameter estimation is important and cannot be ignored.

The paper is organized as follows. In Sec. II we discuss the detection prospects, astrophysical merger rates, and formation channels of eBBH systems. In Sec. III, we describe the waveform models used for eBBH systems, including precessing, aligned-spin and no-spin configurations. Section IV provides an overview of the Bayesian parameter estimation methodology used in our analysis. Section V presents our results, including the impact of eccentricity and spin on parameter recovery. Finally, Sec. VI summarizes our conclusions and highlights prospects for future studies.

II. EBBH: DETECTION, ASTROPHYSICAL RATE AND FORMATION CHANNELS

Detecting gravitational waves from eBBHs presents several unique challenges. The waveform for an eBBH merger can significantly deviate from the quasi-circular inspiral–merger–ringdown (IMR) models that are currently used in traditional matched-filter searches, particularly for lower masses and moderate to high eccentricities. Matched-filter pipelines, such as PyCBC [41–43] and GstLAL [44–46], that use aligned-spin, quasi-circular templates are therefore expected to have reduced sensitivity to eccentric mergers [47]. There have been recent efforts to incorporate eccentricity into template bank searches for binary neutron star, neutron star-black hole mergers [48, 49], and more recently, BBH systems [50]. Additionally, a recent study performed a targeted template based eccentric search for the neutron star-black hole binary GW200105 [51], a binary system for which several works have suggested the presence of significant residual eccentricity [52–54]. However, these searches remain computationally expensive and are typically limited to moderate eccentricities.

As a result, eBBH detection efforts have increasingly relied on model-agnostic search algorithms that are less sensitive to waveform mismatches and can hence capture a broader range of signal morphologies. In particular, the coherent WaveBurst (cWB) algorithm [55–57], which is designed to identify coherent excess power across multiple detectors without strict reliance on waveform templates, is demonstrated to have comparable sensitivity in recovering signals from eBBH systems [13, 14]. While cWB does not perform parameter estimation in the same way as Bayesian inference pipelines, it plays an important role in identifying signatures of eccentricity [58] as well as constraining the merger rates [13, 14]. Furthermore, injections of numerical relativity and semi-analytic eccentric waveforms into detector noise have demonstrated that such unmodeled searches can recover eBBH signals even when eccentricity is moderate to high [59].

Estimating the astrophysical merger rate of eccentric binary black holes remains a challenge, due to the lack of confirmed detections and the complexity of modeling such systems. Current estimates of the eBBH merger rate [14] have been derived from the sensitivity of un-

modeled search pipelines [60] using data from the first three observing runs of LVK, with upper limits remaining several orders of magnitude higher than the rate inferred for circular binaries under the assumption that no eccentric binaries were detected [13]. These constraints place bounds on the population of highly eccentric systems and can be used to validate the predictions of various dynamical formation models by ruling out astrophysical models that predict merger rates that are greater than the upper limits derived from the search sensitivities [13].

Several recent works have also focused on the detectability of eBBH mergers with current gravitational-wave detectors. Ref. [61] investigates the observability of eBBH mergers with current detector sensitivity in a population of simulated BBH mergers from globular cluster. Refs. [62, 63] show the effect of not including eccentricity in population inference and show no significant evidence of eccentricity in population inference using real events.

III. WAVEFORMS FOR EBBH SYSTEM

While quasi-circular binary systems have been extensively studied in both analytical and numerical frameworks throughout the years, their eccentric counterparts have received comparatively limited attention. This disparity is largely due to the astrophysical expectation that eccentricity is efficiently radiated away during the inspiral of comparable-mass compact binaries [31].

From the numerical relativity (NR) perspective, the volume of publicly available simulations of eccentric binaries is modest. The Simulating eXtreme Spacetimes (SXS) collaboration has just recently released more than 200 new simulations of binary black holes (BBHs) with initial eccentricities up to ~ 0.7 [64–66]; the Rochester Institute of Technology (RIT) group has contributed roughly eight hundred short-duration BBH simulations [67], which, while limited in length, are still informative for modeling the merger regime [68, 69]. Additional simulations include ~ 100 cases from the Maya catalog [70] and a small number of eccentric binary neutron stars (BNSs) evolutions available through the CoRe database [71]. These figures contrast starkly with the thousands of quasi-circular (or quasi-spherical) BBH simulations, including those with spin precession, highlighting the relatively under-explored nature of bound, non-circular configurations in NR.

On the analytical side, early developments in post-Newtonian (PN) calculations date back to [72]. The quasi-Keplerian (QK) parameterization formulated by Damour and Deruelle in the 1980s [73] highlighted foundational issues such as the non-uniqueness and gauge dependence of eccentricity in general relativity. The QK formalism has since been extended up to 4PN order for conservative dynamics [74–77], and to 3PN for radiation-reaction contributions [20, 78, 79]. However, fully analytical waveform models remain limited to the inspiral phase [80–84], though merger-ringdown completions can

be attached [77, 85–88].

In the context of the Effective-One-Body (EOB) formalism, since the effective Hamiltonian is based on the re-mapping of full PN-expanded ADM results, non-circular contributions to the conservative dynamics have always been accounted for, starting from the original work by Buonanno and Damour [89]. Extending models to eccentric binaries, then, primarily involves the generalization of radiation-reaction forces and the related waveform multipoles. Initial work in this direction includes the studies by Bini and Damour [90] and Hinderer and Babak [91], the latter also proposing a reparameterization of the EOB dynamics in terms of orbital elements. More sophisticated models have since emerged, such as the SEOBNRE family [92–94], TEOBRESUMS–DALÍ [95–98], and the SEOBNRv4EHM and SEOBNRv5EHM models [20, 21, 99]. Phenomenological models have also begun development, providing a less accurate description of the waveform (with respect to EOB-based waveforms) in exchange for increased speed in waveform generation [100, 101]. Finally, NR surrogates have been built from both EOB waveforms as well as simulations, though for the moment mainly limited to non-spinning binary systems [102–105].

In this work, we employ TEOBRESUMS–DALÍ, the latest extension of the TEOBRESUMS family tailored for eccentric inspirals. In this model, eccentricity is explicitly introduced only through the construction of initial conditions, after which the system evolves using the canonical EOB variables. Non-circular effects in both radial and azimuthal radiation-reaction components are implemented following the approach described in Ref. [95, 106]. The model was validated against a large and diverse set of NR simulations, including quasi-circular, eccentric, and precessing BBHs and BNS [24], finding it more than 99% accurate over a considerable portion of the parameter space. Additional studies have further investigated its accuracy, limiting its applicability to systems with initial eccentricity $\sim 0.6 - 0.7$ [21, 59].

IV. OVERVIEW OF BAYESIAN PARAMETER ESTIMATION METHOD

The physical parameters are estimated for the detected CBC signal, including the masses, spins, luminosity distance, sky position, and other parameters. This estimation is commonly carried out using Bayesian stochastic sampling methods [107]. The primary aim is to construct a posterior distribution $p(\boldsymbol{\theta}|\mathbf{d})$, where $\boldsymbol{\theta} = \{\theta_1, \theta_2, \dots, \theta_p\}$ is the set of model parameters $m = 15$ (for a CBC system) and $\mathbf{d} = \{d_1, d_2, \dots, d_n\}$ is the strain data from a n network of gravitational-wave detectors. Based on Bayes' theorem, the posterior distribution is given by

$$p(\boldsymbol{\theta}|\mathbf{d}) = \frac{\mathcal{L}(\mathbf{d}|\boldsymbol{\theta})\pi(\boldsymbol{\theta})}{p(\mathbf{d}|\mathcal{H})} = \frac{\mathcal{L}(\mathbf{d}|\boldsymbol{\theta})\pi(\boldsymbol{\theta})}{\int \mathcal{L}(\mathbf{d}|\boldsymbol{\theta})\pi(\boldsymbol{\theta})d\boldsymbol{\theta}} \quad (1)$$

where $\mathcal{L}(\mathbf{d}|\boldsymbol{\theta})$ is the likelihood function, the conditional probability density function of the data given the parameters $\boldsymbol{\theta}$. The likelihood function assuming Gaussian noise is taken to be

$$\mathcal{L}(\mathbf{d}|\boldsymbol{\theta}) \propto \exp\left(-\frac{1}{2} \langle \mathbf{d} - h(\boldsymbol{\theta}) | \mathbf{d} - h(\boldsymbol{\theta}) \rangle\right) \quad (2)$$

where $h(\boldsymbol{\theta})$ is the model at given $\boldsymbol{\theta}$, $\langle \cdot | \cdot \rangle$ is a scalar product defined as $\langle a | b \rangle = 4\Re \int_0^\infty \frac{a^*(f)b(f)}{S_n(f)} df$ with S_n being the noise power spectral density of the given GW detector. a^* is the complex conjugate of a , and $\pi(\boldsymbol{\theta})$ is the prior probability density function. Therefore, this is simply a normalization constant with respect to the posterior distribution of $\boldsymbol{\theta}$.

Within the Bayesian framework, all inference is performed conditional on a specific model hypothesis \mathcal{H} , which defines the underlying assumptions about the signal morphology and parameter space (m). Where $\pi(\boldsymbol{\theta}|\mathcal{H})$ is the prior probability density function that encodes our prior knowledge about the parameters within the context of model \mathcal{H} . The model waveform is denoted as $h(\boldsymbol{\theta}|\mathcal{H})$, representing the predicted gravitational wave signal for given parameters $\boldsymbol{\theta}$ under the assumptions of \mathcal{H} . This conditional formulation naturally extends to model comparison, where we can evaluate the relative support for different hypotheses by computing Bayes factors between competing models.

Here, m represents the dimension of the parameter space. As m increases, computing marginal distributions of the Bayesian posterior becomes increasingly difficult because it involves solving high-dimensional integration problems. In order to solve this problem, we can use the simulation-based computational techniques such as Markov Chain Monte Carlo or nested sampling. To get posteriors for free parameters $\boldsymbol{\theta}_f$, we need to marginalize over other parameters $\boldsymbol{\theta}_o$ as $p(\boldsymbol{\theta}_f|\mathbf{d}) = \int p(\boldsymbol{\theta}|\mathbf{d})d\boldsymbol{\theta}_o$. In this analysis, we use the Bilby parameter estimation pipeline [108]. This pipeline is widely used in the GW community due to its flexibility and extensible framework for Bayesian parameter estimation. Built upon modular components that interface with waveform models from LALSuite [109] and other gravitational wave software libraries, Bilby allows users to define likelihood functions and priors while accessing a variety of nested sampling and MCMC techniques through backends such as Dynesty [110], CPNest [111], emcee [112], and PyMultiNest [113]. This allowed us to utilise the eBBH waveforms, which are accessible outside the LALSuite framework. Bilby's strength lies in its ability to marginalise over calibration errors, include arbitrary priors, and efficiently parallelise large sampling jobs across HPC environments. The adoption of Bilby in recent observation runs (e.g., GWTC-3) [114] underscores its reliability and interpretability, especially when used in conjunction with stochastic samplers that map the high-dimensional likelihood surfaces characteristic of binary black hole or neutron star mergers. PE analyses that employ eccen-

Parameter	Value
q	1
D_L	410Mpc
θ_{jn}	0.4 rad
ψ	2.659 rad
ϕ	1.3 rad
RA	1.375 rad
DEC	-1.2108 rad
t_{geocent}	1126259642.413 s

TABLE I: List of parameters that are fixed for all the injected parameters.

tric waveform models typically introduce two additional parameters compared to non-eccentric models, such as eccentricity and mean anomaly. Here we use nested sampling [115], which is implemented in the Bilby sampler. We can also calculate the Bayes factor, which is defined as the ratio of the Bayesian evidence for two competing hypotheses \mathcal{H}_1 and \mathcal{H}_2 , and it is given by $\mathcal{B}_{12} = \frac{p(d|\mathcal{H}_1)}{p(d|\mathcal{H}_2)}$, where $p(d|\mathcal{H})$ is the Bayesian evidence, obtained by marginalising the likelihood over the model parameters, see Eq. (1). A Bayes factor greater than unity indicates preference for \mathcal{H}_1 , whereas a value less than unity favours \mathcal{H}_2 . In the case of systematic studies, we compute the Bayes factor between different configuration setups to understand which configuration has strong evidence for the injected eccentric system.

V. RESULTS

In order to investigate the systematic effects of orbital eccentricity on parameter estimation in the eBBH parameter space, we perform a set of injections using the TEOBRESUMS-DALÍ waveform model [95–98]. Each system is injected with an initial eccentricity in the range $0 \leq e \leq 0.5$ at 5 Hz that varies in steps of 0.1. The mass ratio is fixed to 1 for all injections while the total mass varies in the range $20 M_\odot \leq M \leq 80 M_\odot$ in steps of $10 M_\odot$. We mainly focus on the mass space, which refers to the component-mass parameter space of the binary system, with particular focus on the $30 - 40 M_\odot$ range where the Rate & Population distribution exhibits a pronounced peak [116]. We also estimate eccentricity at 10 Hz using the standard definition, which is discussed in Section 2.1 in [14]. These signals are injected with zero noise into a two-detector network configuration consisting of Hanford and Livingston with design sensitivities [117]. The sky position for these injections is fixed to an arbitrary location, as listed in Table I.

We primarily look at recovered posterior distributions for the component masses and the chirp mass $\mathcal{M} = \frac{(m_1 m_2)^{3/5}}{(m_1 + m_2)^{1/5}}$, and the luminosity distance D_L . We also look at the posterior distributions for the two spin parameters χ_p and χ_{eff} . χ_p is the spin precession parameter [118, 119] which measures the spin effect in the plane

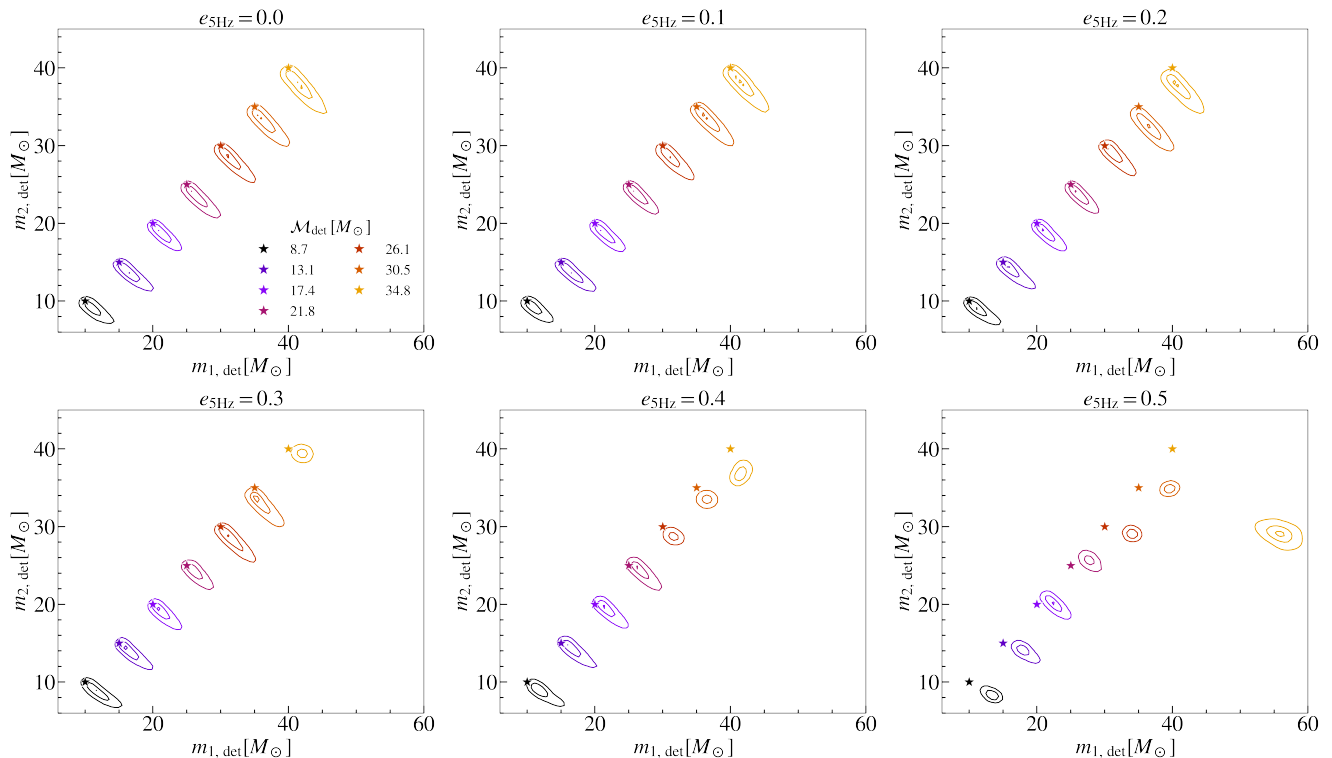


FIG. 1: Posterior distributions of detector-frame component masses m_1 versus m_2 from parameter estimation using a precessing-spin waveform model, for injections with varying initial eccentricities. The injected signals are for eccentric, non-spinning systems, while the recovery uses non-eccentric waveforms with non-aligned component spins, that lead to spin-precession. Each subplot corresponds to an injected eccentricity, ordered increasingly. Star markers indicate the injected m_1 and m_2 values. The 90%, 50%, and 10% credible regions are shown in the plots, and the injected detector-frame chirp mass \mathcal{M} is listed in the legend.

of the binary orbit. It is defined as

$$\chi_p = \max \left(\chi_{1\perp}, \frac{4q+3}{4+3q} q \chi_{2\perp} \right) \quad (3)$$

where, $q = m_2/m_1$ is mass ratio, $\chi_{1\perp} = \chi_1 \sin \theta_1$ and $\chi_{2\perp} = \chi_2 \sin \theta_2$. $\chi_1 = c|\vec{S}_1|/Gm_1^2$ and $\chi_2 = c|\vec{S}_2|/Gm_2^2$. θ_1 and θ_2 are the angles between the orbital angular momentum and the spin vectors \vec{S}_1 and \vec{S}_2 respectively. The other is the effective spin parameter χ_{eff} [120, 121] which measures the effect of spin in the direction of the orbital angular momentum and is defined as

$$\chi_{\text{eff}} = \frac{m_1 \chi_{1\parallel} + m_2 \chi_{2\parallel}}{m_1 + m_2} \quad (4)$$

where, $\chi_{1\parallel} = \chi_1 \cos \theta_1$ and $\chi_{2\parallel} = \chi_2 \cos \theta_2$.

A. Recovery with quasi-circular spinning BBH waveform model (IMRPhenomXPHM)

Parameter estimation is carried out using the Bilby framework as discussed in Sec IV with IMRPhenomXPHM [122, 123], a precessing frequency-domain waveform model that assumes circular orbits and includes the

inspiral, merger, and ringdown phases but no eccentricity. For this study, we limit ourselves to the dominant mode only, excluding the effects of higher modes for both injection and recovery. We performed the analysis using three different recovery parameter setups: one with spin precession, a second with an aligned-spin and a third with a no-spin.

Each injection is analysed using a prior distribution on the binary parameters, carefully selected to ensure sufficient sampling of the relevant parameter space. Specifically, we adopt priors that are uniform in spin magnitudes and redshifted component masses, isotropic in spin orientations, sky location, and binary orientation, and a power law prior on luminosity distance.

Figures 1 and 2 show the credible interval contours for all injections in the detector frame component-mass plane for the precessing-spin and no-spin recoveries, respectively. Each subplot corresponds to a fixed eccentricity, arranged in increasing order of eccentricity. For each eccentricity, we considered seven different equal mass binaries with total masses $M_{\text{det}} = m_{1,\text{det}} + m_{2,\text{det}}$ ranging from $20 M_\odot$ to $80 M_\odot$. For each injection, we display the 90%, 50%, and 10% probability density credible regions obtained from parameter estimation, with the in-

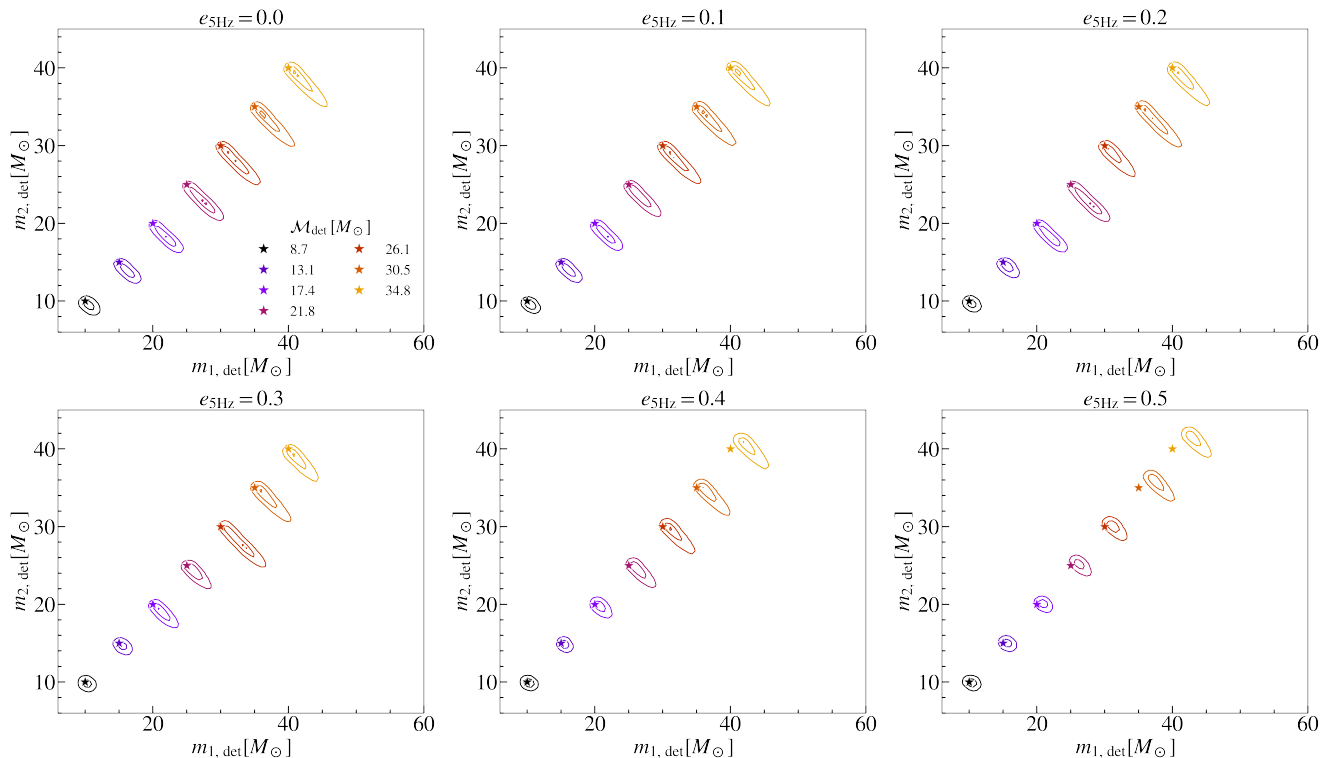


FIG. 2: Posterior distributions of detector-frame component masses m_1 versus m_2 from parameter estimation using a non-spinning waveform model, for injections with varying initial eccentricities. The injected signals are eccentric and non-spinning, while the recovery uses non-eccentric waveforms with no component spins. Each subplot corresponds to an injected eccentricity, ordered increasingly. Star markers indicate the injected m_1 and m_2 values. The 90%, 50%, and 10% credible regions are shown, and the injected detector-frame chirp mass \mathcal{M} is listed in the legend.

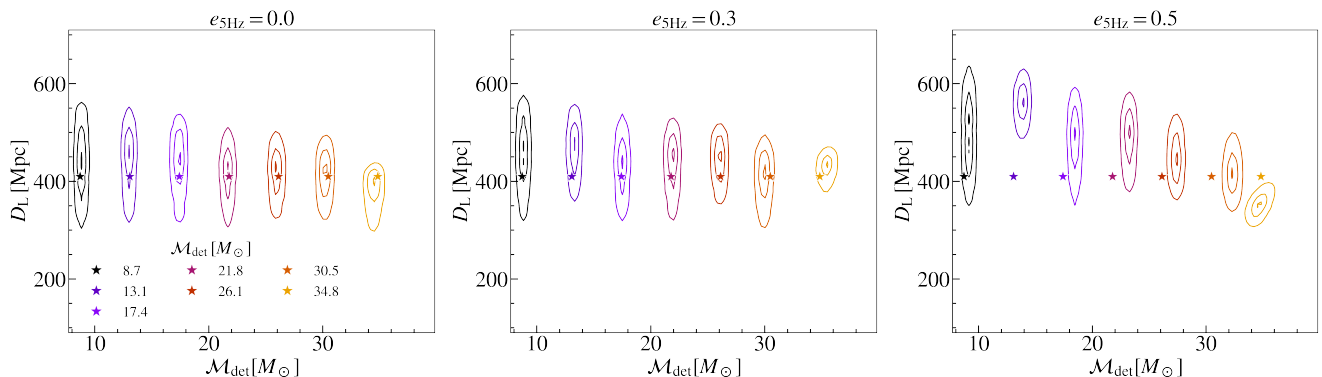


FIG. 3: Posterior distributions of the luminosity distance (D_L) versus chirp mass (\mathcal{M}) from parameters estimation using a precessing-spin waveform model, for injections with varying initial eccentricities. The star markers indicate the injected chirp mass values (\mathcal{M}). The contours represent the 90%, 50%, and 10% credible intervals obtained from parameter estimation.

jected values marked by a star of the same color. The legend indicates the injected detector-frame chirp mass \mathcal{M}_{det} . The first subplot in each plot serves as a reference case, where the injection was performed using the TEOBRESUMS-DALÍ waveform with $e_{5\text{Hz}} = 0$, and the recovery was carried out using the IMRPhenomXPHM waveform model. In no-spin parameter-estimation re-

covery, the inferred masses are generally consistent with the injected masses. Although the recovered values do not exactly match the injected value, the injected parameters lie within the 90% credible interval in most cases. In both configurations, we can see that the deviation is a function of both eccentricity and total mass. For high-mass systems, the posterior distributions of the

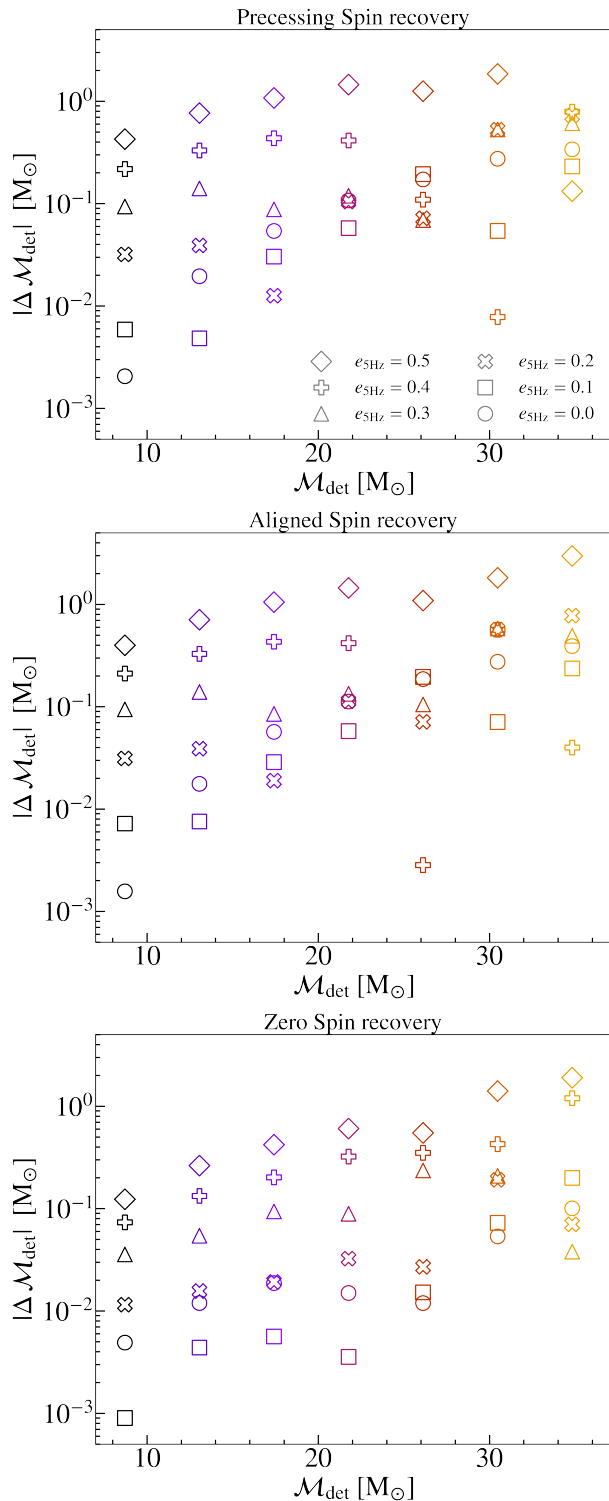


FIG. 4: Absolute differences in chirp mass, $|\Delta\mathcal{M}|$, as a function of the injected chirp mass, \mathcal{M} , for all injections. Here, $\Delta\mathcal{M}$ is defined as the difference between the injected chirp mass and the median of the recovered posterior distribution. The top, middle, and bottom panels correspond to the precessing-spin, aligned spin, and non-spinning configurations respectively. Different marker styles indicate the injected eccentricity. Larger differences are seen for higher eccentricity, while for a given eccentricity the differences increase with increasing injected chirp mass.

component masses begin to show clear deviations even at relatively low injected eccentricities. In contrast, for lower-mass systems, comparable deviations in the mass posteriors only appear at higher injected eccentricities. We observe larger deviations for precessing recovery compared to the non-spinning configuration. We see a similar trend in the deviations for aligned spin recovery as well. The deviation tends to increase for high-mass systems and is smaller for low-mass binaries, with the injected values lying outside the contours for systems with $\mathcal{M}_{\text{det}} > 40 M_{\odot}$. In the precessing recovery setup (numerical values in Table II), we observe a significant deviation from the injected values for systems with $e_{5\text{Hz}} > 0.3$, corresponding to $e_{10\text{Hz}} \approx 0.15$. The deviation initially appears in high-mass systems and, with increasing eccentricity, becomes evident in lower-mass systems as well. This trend suggests that the deviation is directly correlated with both the total mass and the eccentricity of the system. The contribution of the mass ratio was not explored in the present study. The observed behavior differs slightly from the no-spin case, primarily due to the influence of the effective precession spin parameter (χ_p). In Table II of Appendix A, we list the median recovered values along with the 90% bounds for the various recovered parameters for precessing recovery.

For the same parameter estimation runs, we also studied the deviations in the inferred chirp mass in detector frame \mathcal{M}_{det} and the inferred luminosity distance D_L . In Figures 3 and 5 we plot the recovered posteriors of \mathcal{M}_{det} and D_L for precessing and non-spinning configurations, respectively. The labeling and color scheme follow the same convention as in the previous plots. These figures show the credible region contour for all injections, where the stars denote the injected values. We see that for recovery with the precessing waveform model, the injected values of chirp mass and luminosity distance are largely recovered except when $\mathcal{M}_{\text{det}} \geq 13 M_{\odot}$ for $e_{5\text{Hz}} = 0.5$. We show only three cases of initial eccentricity $e_{5\text{Hz}}$ to better understand this behavior. For recovery with a non-spinning waveform model, the injected values of the chirp mass and luminosity distance are recovered for all cases up to $e_{5\text{Hz}} = 0.4$. For $e_{5\text{Hz}} = 0.5$, the injected values of the chirp mass and luminosity distance for systems with $\mathcal{M}_{\text{det}} \geq 30 M_{\odot}$ are not recovered. We observe a significant difference between the precessing and non-spinning configurations in this parameter space at high eccentricity.

To understand this clearly, we have plotted the absolute deviation in the mass parameter space, specifically the deviations in the chirp mass \mathcal{M}_{det} . Figure 4 shows the absolute deviation in the chirp mass \mathcal{M}_{det} between the injected value and the median value of the posterior distribution. The top, middle and bottom panels correspond to the recovery with precessing spin, aligned spin and non-spinning waveforms, respectively. We observe two key trends associated with changes in mass and eccentricity. Systems with lower eccentricity have an overall smaller deviation compared to systems with

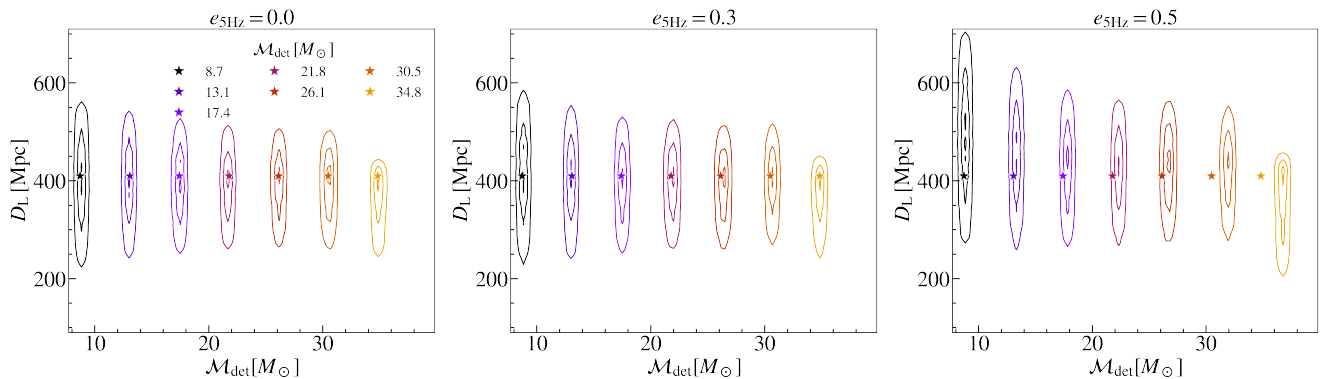


FIG. 5: Posterior distributions of the luminosity distance (D_L) versus chirp mass (\mathcal{M}) from parameter estimation using a non-spinning waveform model, for injections with varying initial eccentricity. The star markers indicate the injected chirp mass values (\mathcal{M}). The contours represent the 90%, 50%, and 10% credible intervals obtained from parameter estimation.

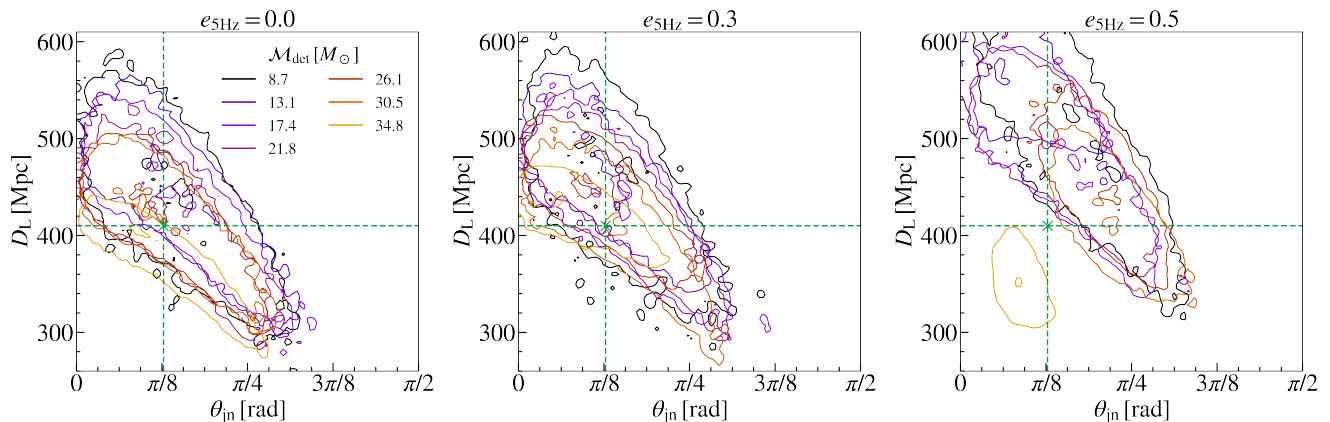


FIG. 6: Posterior distributions of the luminosity distance (D_L) versus inclination angle (θ_{jn}) from parameter estimation of injected signal with varying eccentricities, using a precessing waveform model. The contours represent 95% and 5% credible intervals. The dotted green line indicates the injected values.

larger eccentricity. For a given injected eccentricity, the deviations increase as the total mass of the binary is increased. Larger deviations are observed in the case of aligned/precessing spin configurations compared to the non-spinning case, which is mainly due to the modulation introduced by spin parameters.

In Figure 6, we plot inclination angle versus the luminosity distance posterior samples. We see that the systems with high eccentricity, when recovered using a precessing waveform model, exhibit a shift in the recovered inclination angle θ_{jn} towards an edge-on system. Note that we use the same labeling and color scheme for the contours as in the other figures; however, the injected values of luminosity distance and inclination angle are the same, and are denoted by green dashed lines.

Figure 10 in Appendix B shows the posterior distributions of the precessing component spin parameter χ_P for different eccentric injections when recovered using a precessing spin waveform. There is an overall increase in the support for precessing spins across all injected masses

as the value of the initial eccentricity increases. As the eccentricity is increased, the χ_P posterior distributions shift to larger values and become narrower. For eccentricities up to 0.2, we see that the distributions of χ_P favor a low precessing spin. For $e_{5Hz} = 0.3$ and above, the posteriors favor high precessing spins. In the case of χ_{eff} recovery as shown in Figure 11 in Appendix B, we see that for low to moderate initial eccentricity, the recovered median values are close to zero. For $e_{5Hz} \geq 0.4$ we see that the recovered values are non-negligible.

To quantify these recoveries and determine which one best represents the multi-dimensional parameter space, we calculate \mathcal{B} between two hypotheses, circular precessing recovery (\mathcal{H}_P) and circular non-spinning recovery (\mathcal{H}_{NS}). Figure 7 shows the estimated \mathcal{B} for all simulations with varying masses and eccentricities. $\mathcal{B} > 1$ indicates precessing recovery has stronger support compared to non-spinning recovery. We also noticed that as eccentricity increases, \mathcal{B} also increases. Additionally, we observed that this trend is not strongly dependent on

chirp mass.

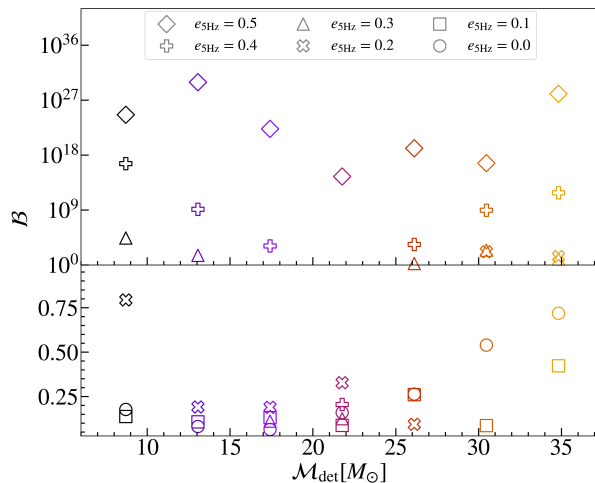


FIG. 7: Bayes factor \mathcal{B} calculated between precessing spin and non-spinning recovery of simulated equal-mass non-spinning eccentric systems with various chirp masses (horizontal axis) and eccentricities (symbols). The plot is split into two panels about $\mathcal{B} = 1$. $\mathcal{B} > 1$ indicates that a precessing spin recovery of the injection is preferred over the no spin recovery.

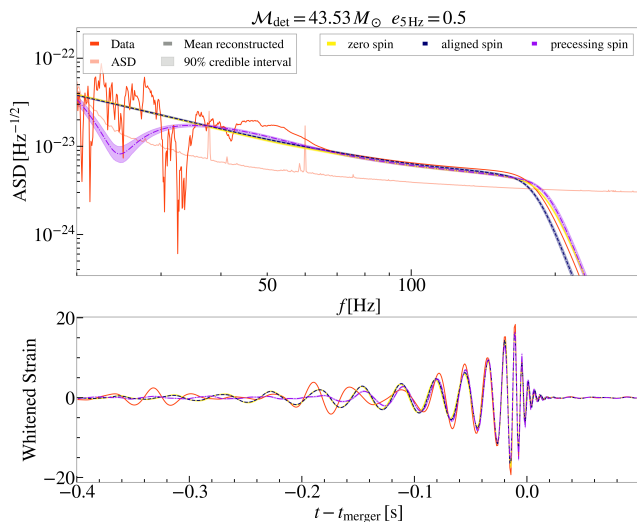


FIG. 8: Waveform reconstruction for the three circular recovery with no spin, and spin (aligned and precessing) plotted against the injected signal. All the waveforms recover the late inspiral and merger part of the signal well.

In figure 8 we show the reconstructed waveform as well as the injected waveform in frequency domain (top panel) and time domain (bottom panel) for an injection with eccentricity $e_{5\text{Hz}} = 0.5$. The solid red line represents

data with an injected signal. Yellow, dashed black, and violet-colored lines correspond to non-spinning, aligned spin, and precessing spin waveforms, respectively. This plot shows that all recovery configurations recover the late inspiral and merger part of the signal better than the early inspiral part.

B. Recovery with eccentric aligned spin binary black hole waveform model: TEOBRESUMS-DALÍ

We have injected a non-spinning equal mass binary with $\mathcal{M} = 26.1M_\odot$ and $e_{20\text{Hz}} = 0.1$, with all other parameters fixed as the same as previous injections. Here, we have recovered using the eccentric waveform model TEOBRESUMS-DALÍ, where we have employed a uniform prior on eccentricity. Note that the recovered eccentricity is estimated at $f_{ref} = 20$ Hz. For these parameter estimations, we have used a slightly different range of priors compared to the runs in the previous section. Figure 9 shows the posterior distributions for parameters such as chirp mass, mass ratio, eccentricity and distance with TEOBRESUMS-DALÍ. The injected values are indicated by the orange vertical lines. We also perform parameter estimation on this system with a precessing IMRPHENOMXPHM in order to calculate the Bayes factor between the two runs. We find that the Bayes factor between precession recovery w.r.t eccentricity recovery is $\mathcal{B}_{PE} = 1.18 \times 10^{-7}$. This indicates eccentric recovery is more accurate in multi-dimensional parameters. This example highlights the importance of using eccentric waveform models for reliable parameter estimation of such sources. We plan to analyze selected special events with this model in future work.

VI. CONCLUSION

In this study, we systematically investigated the impact of orbital eccentricity on parameter estimation and the biases introduced when this effect is ignored. We utilized the TEOBRESUMS-DALÍ model to simulate eccentric non-spinning systems as injections and the IMRPHENOMXPHM model of circular (non-eccentric) systems for recovery. We use three different configurations, namely, the precessing case (involving non-aligned component spins), the non-precessing case (involving spins aligned with the orbital angular momentum) and the non-spinning case (where all spin components are set to be zero). Our analysis covered a broad range of binary black hole masses ($20 M_\odot$ – $80 M_\odot$) and eccentricities ($0 \leq e_{5\text{Hz}} \leq 0.5$) and revealed that the accuracy of recovered parameters strongly depends on both total mass and eccentricity. Especially for high-mass systems, the posterior distributions of the component masses begin to show clear deviations even at relatively low injected eccentricities. But in the case of lower-mass systems, comparable deviations in the mass posteriors only

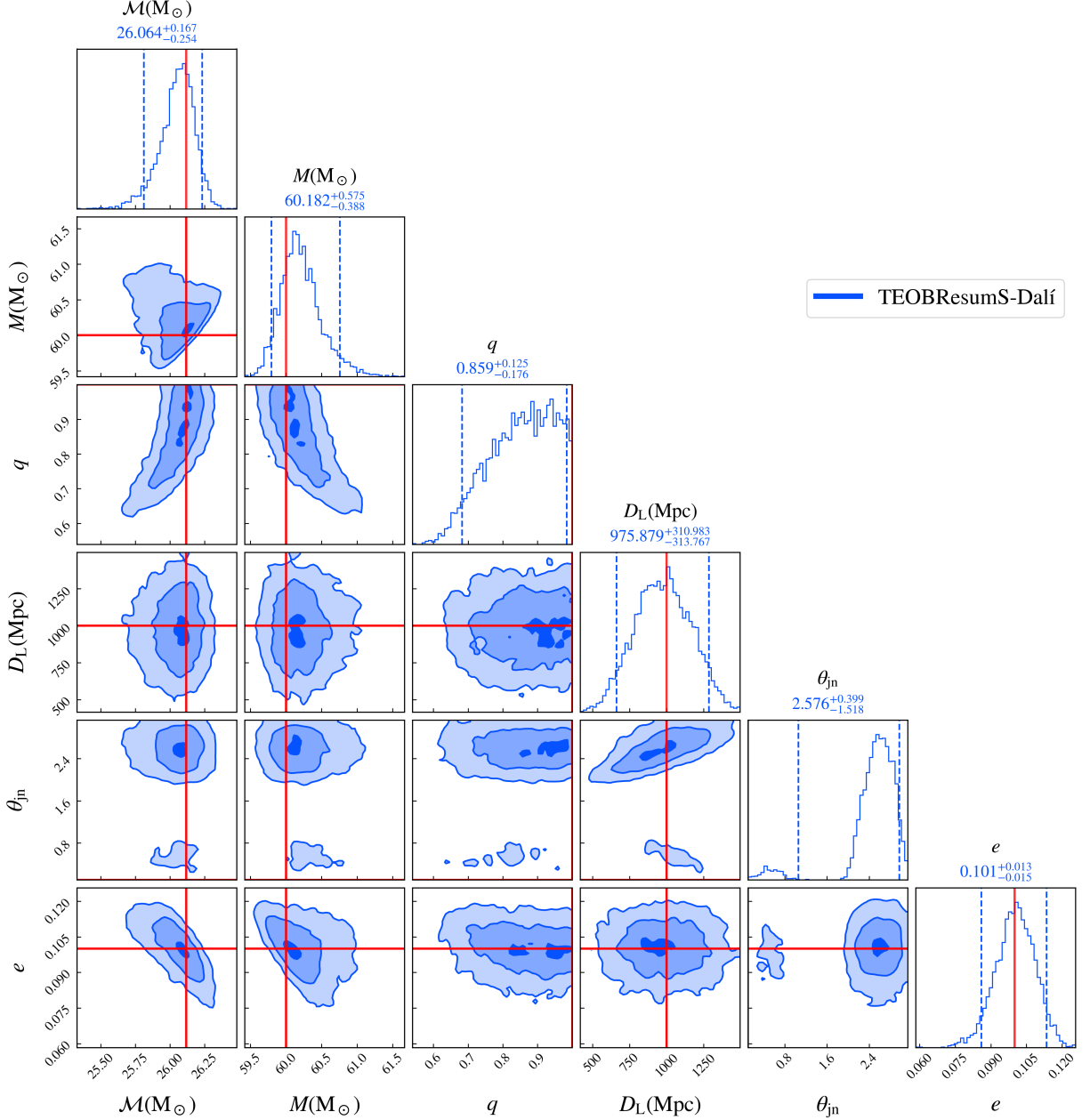


FIG. 9: Posterior samples from parameter estimation of a non-spinning eccentric signal injected and recovered using TEOBRESUMS–DALÍ. Red lines indicate the injected parameter values. Median recovered value with 90% credible intervals quoted above each parameter posterior plot.

appear at higher injected eccentricities. For low eccentricities ($e_{5\text{Hz}} < 0.3$), the injected parameters were generally recovered within the 90% credible intervals. However, we observe deviations in the recovered parameters as the eccentricity is increased. In particular, systems with $e_{5\text{Hz}} > 0.4$ and total masses above $40 M_{\odot}$ showed significant discrepancies in the recovered chirp mass, spin precession, and luminosity distance.

In this paper, we also demonstrated that using the TEOBRESUMS–DALÍ waveform model (which is applicable for eccentric binary systems) within the Bilby

framework allows us to recover eccentricity well. Using this setup, we can reliably estimate the source parameters of events, including the eccentricity.

These findings suggest that waveform models that assume circular orbits, such as IMRPhenomXPHM, lose accuracy when applied to gravitational-wave signals from highly eccentric mergers, particularly in the high-mass regime. The observed bias in parameters such as inclination and precessing spin further underscores the interplay between eccentricity and spin precession, which can lead to misinterpretation of astrophysical parameters if eccen-

tricity is neglected.

In future work, we plan to extend this systematic study to higher masses, as well as the high-spin and high-mass-ratio space. Additionally, we plan to conduct a study to evaluate the effect of these biases when including higher-order modes. This will result in a better understanding of where we can ignore eccentricity in parameter estimation for real events. Incorporating next-generation eccentric waveform models into parameter estimation pipelines will be crucial to improve source characterization for upcoming observing runs as well as to understand the origin of these binaries.

VII. ACKNOWLEDGEMENT

We gratefully acknowledge the support of LIGO and Virgo for the provision of computational resources. G.V. and T.R.C acknowledge the support of the National Science Foundation under grant PHY-2207728 and PHY-2513124. I.B. acknowledges the support of the National

Science Foundation under grants #1911796, #2110060 and #2207661 and of the Alfred P. Sloan Foundation. We would like to thank Pratyusava Baral for useful comments on the manuscript.

This research has made use of data, software and/or web tools obtained from the Gravitational Wave Open Science Center (<https://www.gw-openscience.org>), a service of LIGO Laboratory, the LIGO Scientific Collaboration and the Virgo Collaboration. LIGO is funded by the U.S. National Science Foundation. Virgo is funded by the French Centre National de Recherche Scientifique (CNRS), the Italian Istituto Nazionale della Fisica Nucleare (INFN) and the Dutch Nikhef, with contributions by Polish and Hungarian institutes. This material is based upon work supported by NSF’s LIGO Laboratory, which is a major facility fully funded by the National Science Foundation. Computations were performed in the CIT cluster provided by LIGO Laboratory and Hawk computing center at Cardiff University supported by STFC grant.

This document has a LIGO preprint number LIGO-P2600058.

-
- [1] J. Aasi *et al.*, Advanced LIGO, *Class. Quantum Grav.* **32**, 074001 (2015).
 - [2] F. Acernese *et al.*, Advanced Virgo: a second-generation interferometric gravitational wave detector, *Class. Quantum Grav.* **32**, 024001 (2015).
 - [3] T. Akutsu *et al.* (KAGRA), KAGRA: 2.5 Generation Interferometric Gravitational Wave Detector, *Nature Astron.* **3**, 35 (2019), [arXiv:1811.08079 \[gr-qc\]](https://arxiv.org/abs/1811.08079).
 - [4] B. P. Abbott, R. Abbott, T. D. Abbott, *et al.*, GWTC-1: A Gravitational-Wave Transient Catalog of Compact Binary Mergers Observed by LIGO and Virgo during the First and Second Observing Runs, *Phys. Rev. X* **9**, 031040 (2019).
 - [5] R. Abbott, T. D. Abbott, S. Abraham, *et al.*, GWTC-2: Compact Binary Coalescences Observed by LIGO and Virgo during the First Half of the Third Observing Run, *Phys. Rev. X* **11**, 021053 (2021).
 - [6] R. Abbott *et al.* (LIGO Scientific, VIRGO), GWTC-2.1: Deep extended catalog of compact binary coalescences observed by LIGO and Virgo during the first half of the third observing run, *Phys. Rev. D* **109**, 022001 (2024), [arXiv:2108.01045 \[gr-qc\]](https://arxiv.org/abs/2108.01045).
 - [7] A. G. Abac *et al.* (LIGO Scientific, VIRGO, KAGRA), GW231123: A Binary Black Hole Merger with Total Mass 190-265 M_{\odot} , *Astrophys. J. Lett.* **993**, L25 (2025), [arXiv:2507.08219 \[astro-ph.HE\]](https://arxiv.org/abs/2507.08219).
 - [8] R. Abbott, T. D. Abbott, F. Acernese, *et al.*, GWTC-3: Compact Binary Coalescences Observed by LIGO and Virgo during the Second Part of the Third Observing Run, *Phys. Rev. X* **13**, 041039 (2023).
 - [9] A. G. Abac *et al.* (LIGO Scientific, VIRGO, KAGRA), GWTC-4.0: Updating the Gravitational-Wave Transient Catalog with Observations from the First Part of the Fourth LIGO-Virgo-KAGRA Observing Run, (2025), [arXiv:2508.18082 \[gr-qc\]](https://arxiv.org/abs/2508.18082).
 - [10] R. Abbott, T. D. Abbott, S. Abraham, *et al.*, Gw190521: A binary black hole merger with a total mass of 150 M_{\odot} , *Phys. Rev. Lett.* **125**, 101102 (2020).
 - [11] B. P. Abbott *et al.* (KAGRA, LIGO Scientific, Virgo, VIRGO), Prospects for observing and localizing gravitational-wave transients with Advanced LIGO, Advanced Virgo and KAGRA, *Living Rev. Rel.* **21**, 3 (2018), [arXiv:1304.0670 \[gr-qc\]](https://arxiv.org/abs/1304.0670).
 - [12] R. W. Kiendrebeogo *et al.*, Updated Observing Scenarios and Multimessenger Implications for the International Gravitational-wave Networks O4 and O5, *Astrophys. J.* **958**, 158 (2023), [arXiv:2306.09234 \[astro-ph.HE\]](https://arxiv.org/abs/2306.09234).
 - [13] B. P. Abbott, R. Abbott, T. D. Abbott, S. Abraham, F. Acernese, K. Ackley, C. Adams, R. X. Adhikari, V. B. Adya, *et al.*, Search for eccentric binary black hole mergers with advanced LIGO and advanced virgo during their first and second observing runs, *Astrophys. J.* **883**, 149 (2019).
 - [14] A. G. Abac *et al.* (LIGO Scientific, KAGRA, VIRGO), Search for Eccentric Black Hole Coalescences during the Third Observing Run of LIGO and Virgo, *Astrophys. J.* **973**, 132 (2024), [arXiv:2308.03822 \[astro-ph.HE\]](https://arxiv.org/abs/2308.03822).
 - [15] H. L. Iglesias *et al.*, Eccentricity Estimation for Five Binary Black Hole Mergers with Higher-order Gravitational-wave Modes, *Astrophys. J.* **972**, 65 (2024), [arXiv:2208.01766 \[gr-qc\]](https://arxiv.org/abs/2208.01766).
 - [16] N. Gupte *et al.*, Evidence for eccentricity in the population of binary black holes observed by LIGO-Virgo-KAGRA, *Phys. Rev. D* **112**, 104045 (2025), [arXiv:2404.14286 \[gr-qc\]](https://arxiv.org/abs/2404.14286).
 - [17] V. Gayathri, J. Healy, J. Lange, B. O’Brien, M. Szczepańczyk, I. Bartos, M. Campanelli, S. Klimenko, C. O. Lousto, and R. O’Shaughnessy, Eccentricity estimate for black hole mergers with numerical rel-

- activity simulations, *Nature Astro* [10.1038/s41550-021-01568-w](https://doi.org/10.1038/s41550-021-01568-w) (2022).
- [18] I. M. Romero-Shaw, P. D. Lasky, E. Thrane, and J. C. Bustillo, GW190521: orbital eccentricity and signatures of dynamical formation in a binary black hole merger signal, *Astrophys. J. Lett.* **903**, L5 (2020), [arXiv:2009.04771](https://arxiv.org/abs/2009.04771) [astro-ph.HE].
- [19] R. Gamba, M. Breschi, G. Carullo, S. Albanesi, P. Rettengo, S. Bernuzzi, and A. Nagar, GW190521 as a dynamical capture of two nonspinning black holes, *Nature Astro.* **7**, 11 (2023), [arXiv:2106.05575](https://arxiv.org/abs/2106.05575) [gr-qc].
- [20] A. Gamboa, M. Khalil, and A. Buonanno, Third post-Newtonian dynamics for eccentric orbits and aligned spins in the effective-one-body waveform model seobnr5ehm, *Phys. Rev. D* **112**, 044037 (2025), [arXiv:2412.12831](https://arxiv.org/abs/2412.12831) [gr-qc].
- [21] A. Gamboa *et al.*, Accurate waveforms for eccentric, aligned-spin binary black holes: The multipolar effective-one-body model seobnr5ehm, *Phys. Rev. D* **112**, 044038 (2025), [arXiv:2412.12823](https://arxiv.org/abs/2412.12823) [gr-qc].
- [22] A. Nagar, S. Bernuzzi, *et al.*, Time-domain effective-one-body gravitational waveforms for coalescing compact binaries with nonprecessing spins, tides and self-spin effects, *Phys. Rev. D* **98**, 084001 (2018), [arXiv:1806.01772](https://arxiv.org/abs/1806.01772) [gr-qc].
- [23] A. Nagar, R. Gamba, P. Rettengo, V. Fantini, and S. Bernuzzi, Effective-one-body waveform model for non-circularized, planar, coalescing black-hole binaries: the importance of radiation reaction, *Phys. Rev. D* **110**, 084001 (2024), [arXiv:2404.05288](https://arxiv.org/abs/2404.05288) [gr-qc].
- [24] S. Albanesi, R. Gamba, S. Bernuzzi, J. Fontbuté, A. Gonzalez, and A. Nagar, [Effective-one-body modeling for generic compact binaries with arbitrary orbits](https://arxiv.org/abs/2503.14580) (2025), [arXiv:2503.14580](https://arxiv.org/abs/2503.14580) [gr-qc].
- [25] I. M. Romero-Shaw, P. D. Lasky, and E. Thrane, Searching for Eccentricity: Signatures of Dynamical Formation in the First Gravitational-Wave Transient Catalogue of LIGO and Virgo, *Mon. Not. Roy. Astron. Soc.* **490**, 5210 (2019), [arXiv:1909.05466](https://arxiv.org/abs/1909.05466) [astro-ph.HE].
- [26] V. Cardoso, C. F. B. Macedo, and R. Vicente, Eccentricity evolution of compact binaries and applications to gravitational-wave physics, *Phys. Rev. D* **103**, 023015 (2021).
- [27] M. Zevin, I. M. Romero-Shaw, K. Kremer, E. Thrane, and P. D. Lasky, Implications of Eccentric Observations on Binary Black Hole Formation Channels, *Astrophys. J. Lett.* **921**, L43 (2021), [arXiv:2106.09042](https://arxiv.org/abs/2106.09042) [astro-ph.HE].
- [28] F. Antonini and F. A. Rasio, Merging black hole binaries in galactic nuclei: implications for advanced-LIGO detections, *Astrophys. J.* **831**, 187 (2016), [arXiv:1606.04889](https://arxiv.org/abs/1606.04889) [astro-ph.HE].
- [29] J. Samsing, Eccentric Black Hole Mergers Forming in Globular Clusters, *Phys. Rev. D* **97**, 103014 (2018), [arXiv:1711.07452](https://arxiv.org/abs/1711.07452) [astro-ph.HE].
- [30] J. Samsing, I. Bartos, D. J. D’Orazio, Z. Haiman, B. Kocsis, N. W. C. Leigh, B. Liu, M. E. Pessah, and H. Tagawa, AGN as potential factories for eccentric black hole mergers, *Nature* **603**, 237 (2022), [arXiv:2010.09765](https://arxiv.org/abs/2010.09765) [astro-ph.HE].
- [31] P. C. Peters and J. Mathews, Gravitational radiation from point masses in a Keplerian orbit, *Phys. Rev.* **131**, 435 (1963).
- [32] T. A. Apostolatos, C. Cutler, G. J. Sussman, and K. S. Thorne, Spin induced orbital precession and its modulation of the gravitational wave forms from merging binaries, *Phys. Rev. D* **49**, 6274 (1994).
- [33] R. J. E. Smith, K. Cannon, C. Hanna, D. Keppel, and I. Mandel, Towards Rapid Parameter Estimation on Gravitational Waves from Compact Binaries using Interpolated Waveforms, *Phys. Rev. D* **87**, 122002 (2013), [arXiv:1211.1254](https://arxiv.org/abs/1211.1254) [astro-ph.HE].
- [34] E. A. Huerta, P. Kumar, S. T. McWilliams, R. O’Shaughnessy, and N. Yunes, Accurate and efficient waveforms for compact binaries on eccentric orbits, *Phys. Rev. D* **90**, 084016 (2014), [arXiv:1408.3406](https://arxiv.org/abs/1408.3406) [gr-qc].
- [35] I. M. Romero-Shaw, D. Gerosa, and N. Loutrel, Eccentricity or spin precession? distinguishing subdominant effects in gravitational-wave data, *Monthly Notices of the Royal Astronomical Society* **519**, 5352–5357 (2023).
- [36] E. A. Huerta, R. Haas, S. T. McWilliams, *et al.*, Complete waveform model for eccentric binary black hole mergers, *Physical Review D* **95**, 10.1103/PhysRevD.95.024038 (2017).
- [37] M. Lower, E. Thrane, P. D. Lasky, and E. B. Olsen, Measuring eccentricity in binary black hole inspirals with advanced ligo, *Physical Review D* **98**, 10.1103/PhysRevD.98.083028 (2018).
- [38] A. Ramos-Buades, H. P. Pfeiffer, A. Buonanno, *et al.*, Effect of residual eccentricity in gravitational-wave parameter estimation for binary black holes, *Physical Review D* **101**, 10.1103/PhysRevD.101.083015 (2020).
- [39] E. O’Shea and P. Kumar, Systematic biases in parameter estimation of eccentric binary black holes with circular templates, *Monthly Notices of the Royal Astronomical Society* **508**, 4064 (2021).
- [40] Divyajyoti, I. M. Romero-Shaw, V. Prasad, K. Paul, C. Kant Mishra, P. Kumar, A. Maurya, M. Boyle, L. E. Kidder, H. P. Pfeiffer, and M. A. Scheel, Biased parameter inference of eccentric, spin-precessing binary black holes, *arXiv e-prints*, [arXiv:2510.04332](https://arxiv.org/abs/2510.04332) (2025), [arXiv:2510.04332](https://arxiv.org/abs/2510.04332) [gr-qc].
- [41] B. Allen, W. G. Anderson, P. R. Brady, D. A. Brown, and J. D. E. Creighton, FINDCHIRP: An Algorithm for detection of gravitational waves from inspiraling compact binaries, *Phys. Rev. D* **85**, 122006 (2012), [arXiv:gr-qc/0509116](https://arxiv.org/abs/gr-qc/0509116).
- [42] S. A. Usman *et al.*, The PyCBC search for gravitational waves from compact binary coalescence, *Class. Quant. Grav.* **33**, 215004 (2016), [arXiv:1508.02357](https://arxiv.org/abs/1508.02357) [gr-qc].
- [43] A. H. Nitz, T. Dent, T. Dal Canton, S. Fairhurst, and D. A. Brown, Detecting binary compact-object mergers with gravitational waves: Understanding and Improving the sensitivity of the PyCBC search, *Astrophys. J.* **849**, 118 (2017), [arXiv:1705.01513](https://arxiv.org/abs/1705.01513) [gr-qc].
- [44] C. Messick, K. Blackburn, P. Brady, P. Brockill, K. Cannon, R. Cariou, S. Caudill, S. J. Chamberlin, J. D. E. Creighton, R. Everett, C. Hanna, D. Keppel, R. N. Lang, T. G. F. Li, D. Meacher, A. Nielsen, C. Pankow, S. Privitera, H. Qi, S. Sachdev, L. Sadeghian, L. Singer, E. G. Thomas, L. Wade, M. Wade, A. Weinstein, and K. Wiesner, Analysis framework for the prompt discovery of compact binary mergers in gravitational-wave data, *Phys. Rev. D* **95**, 042001 (2017).
- [45] S. Sachdev *et al.*, The GstLAL Search Analysis Methods for Compact Binary Mergers in Advanced LIGO’s Second and Advanced Virgo’s First Observing Runs,

- (2019), [arXiv:1901.08580 \[gr-qc\]](#).
- [46] P. Joshi *et al.*, New Methods for Offline GstLAL Analyses, (2025), [arXiv:2506.06497 \[gr-qc\]](#).
- [47] D. A. Brown and P. J. Zimmerman, Effect of eccentricity on searches for gravitational waves from coalescing compact binaries in ground-based detectors, *Phys. Rev. D* **81**, 024007 (2010), [arXiv:0909.0066 \[gr-qc\]](#).
- [48] R. Dhurkunde and A. H. Nitz, Search for eccentric NSBH and BNS mergers in the third observing run of Advanced LIGO and Virgo, *Phys. Rev. D* **111**, 103018 (2025), [arXiv:2311.00242 \[astro-ph.HE\]](#).
- [49] K. S. Phukon, P. Schmidt, and G. Pratten, Geometric template bank for the detection of spinning low-mass compact binaries with moderate orbital eccentricity, *Phys. Rev. D* **111**, 043040 (2025), [arXiv:2412.06433 \[gr-qc\]](#).
- [50] Y.-F. Wang and A. H. Nitz, Search for Gravitational Waves from Eccentric Binary Black Holes with an Effective-one-body Template, *Astrophys. J.* **993**, 215 (2025), [arXiv:2508.05018 \[gr-qc\]](#).
- [51] K. S. Phukon, P. Schmidt, G. Morras, and G. Pratten, Detection of GW200105 with a targeted eccentric search, (2025), [arXiv:2512.10803 \[gr-qc\]](#).
- [52] G. Morras, G. Pratten, and P. Schmidt, Orbital eccentricity in a neutron star - black hole binary merger, (2025), [arXiv:2503.15393 \[astro-ph.HE\]](#).
- [53] A. Tiwari, S. A. Bhat, M. A. Shaikh, and S. J. Kapadia, Testing the Nature of GW200105 by Probing the Frequency Evolution of Eccentricity, *Astrophys. J.* **995**, 48 (2025), [arXiv:2509.26152 \[astro-ph.HE\]](#).
- [54] A. Jan, B.-J. Tsao, R. O’Shaughnessy, D. Shoemaker, and P. Laguna, GW200105: A detailed study of eccentricity in the neutron star-black hole binary, *Phys. Rev. D* **113**, 024018 (2026), [arXiv:2508.12460 \[gr-qc\]](#).
- [55] S. Klimentenko, S. Mohanty, M. Rakhmanov, and G. Mitselmakher, Constraint likelihood analysis for a network of gravitational wave detectors, *Phys. Rev. D* **72**, 122002 (2005).
- [56] V. Necula, S. Klimentenko, and G. Mitselmakher, Transient analysis with fast Wilson-Daubechies time-frequency transform, *J. Phys. Conf. Ser.* **363**, 012032 (2012).
- [57] S. Klimentenko, G. Vedovato, M. Drago, F. Salemi, V. Tiwari, G. A. Prodi, C. Lazzaro, K. Ackley, S. Tiwari, C. F. Da Silva, and G. Mitselmakher, Method for detection and reconstruction of gravitational wave transients with networks of advanced detectors, *Phys. Rev. D* **93**, 042004 (2016).
- [58] R. Das, V. Gayathri, Divyajyoti, S. Jose, I. Bartos, S. Klimentenko, and C. K. Mishra, Inferring additional physics through unmodeled signal reconstructions, *Phys. Rev. D* **112**, 023011 (2025), [arXiv:2412.11749 \[gr-qc\]](#).
- [59] S. Bhaumik *et al.*, Gravitational wave detector sensitivity to eccentric black hole mergers, *Phys. Rev. D* **111**, 123032 (2025), [arXiv:2410.15192 \[gr-qc\]](#).
- [60] R. Biswas, P. R. Brady, J. D. E. Creighton, and S. Fairhurst, The Loudest event statistic: General formulation, properties and applications, *Class. Quant. Grav.* **26**, 175009 (2009), [Erratum: *Class. Quant. Grav.* **30**, 079502 (2013)], [arXiv:0710.0465 \[gr-qc\]](#).
- [61] M. K. Singh, B. G. Patterson, and S. Fairhurst, Observability of eccentricity in a population of merging compact binaries, (2025), [arXiv:2512.07688 \[astro-ph.HE\]](#).
- [62] M. Zeeshan and R. O’Shaughnessy, Eccentricity matters: Impact of eccentricity on inferred binary black hole populations, *Phys. Rev. D* **110**, 063009 (2024), [arXiv:2404.08185 \[gr-qc\]](#).
- [63] M. Zeeshan, R. O’Shaughnessy, and N. Malagon, Population Properties of Binary Black Holes with Eccentricity, (2026), [arXiv:2602.11030 \[astro-ph.HE\]](#).
- [64] A. Ramos-Buades, M. van de Meent, H. P. Pfeiffer, H. R. Rüter, M. A. Scheel, M. Boyle, and L. E. Kidder, Eccentric binary black holes: Comparing numerical relativity and small mass-ratio perturbation theory, *Phys. Rev. D* **106**, 124040 (2022), [arXiv:2209.03390 \[gr-qc\]](#).
- [65] M. Boyle *et al.*, The SXS Collaboration catalog of binary black hole simulations, *Class. Quantum Grav.* **36**, 195006 (2019), [arXiv:1904.04831 \[gr-qc\]](#).
- [66] M. A. Scheel *et al.*, The SXS collaboration’s third catalog of binary black hole simulations, *Class. Quant. Grav.* **42**, 195017 (2025), [arXiv:2505.13378 \[gr-qc\]](#).
- [67] J. Healy and C. O. Lousto, Fourth RIT binary black hole simulations catalog: Extension to eccentric orbits, *Phys. Rev. D* **105**, 124010 (2022), [arXiv:2202.00018 \[gr-qc\]](#).
- [68] G. Carullo, S. Albanesi, A. Nagar, R. Gamba, S. Bernuzzi, T. Andrade, and J. Trenado, Unveiling the Merger Structure of Black Hole Binaries in Generic Planar Orbits, *Phys. Rev. Lett.* **132**, 101401 (2024), [arXiv:2309.07228 \[gr-qc\]](#).
- [69] G. Carullo, Ringdown amplitudes of nonspinning eccentric binaries, (2024), [arXiv:2406.19442 \[gr-qc\]](#).
- [70] D. Ferguson *et al.*, Second MAYA catalog of binary black hole numerical relativity waveforms, *Phys. Rev. D* **112**, 044043 (2025), [arXiv:2309.00262 \[gr-qc\]](#).
- [71] A. Gonzalez *et al.*, Second release of the CoRe database of binary neutron star merger waveforms, *Class. Quant. Grav.* **40**, 085011 (2023), [arXiv:2210.16366 \[gr-qc\]](#).
- [72] R. V. Wagoner and C. M. Will, Post-Newtonian gravitational radiation from orbiting point masses., *Astrophys. J.* **210**, 764 (1976).
- [73] T. Damour and N. Deruelle, General relativistic celestial mechanics of binary systems. I. The post-Newtonian motion., *Annales de L’Institut Henri Poincaré Section (A) Physique Theorique* **43**, 107 (1985).
- [74] T. Damour and G. Schaefer, Higher Order Relativistic Periastron Advances and Binary Pulsars, *Nuovo Cim. B* **101**, 127 (1988).
- [75] G. Schäfer and N. Wex, Second post-Newtonian motion of compact binaries, *Physics Letters A* **174**, 196 (1993).
- [76] R.-M. Memmesheimer, A. Gopakumar, and G. Schaefer, Third post-Newtonian accurate generalized quasi-Keplerian parametrization for compact binaries in eccentric orbits, *Phys. Rev. D* **70**, 104011 (2004), [arXiv:gr-qc/0407049](#).
- [77] G. Cho, S. Tanay, A. Gopakumar, and H. M. Lee, Generalized quasi-Keplerian solution for eccentric, nonspinning compact binaries at 4PN order and the associated inspiral-merger-ringdown waveform, *Phys. Rev. D* **105**, 064010 (2022), [arXiv:2110.09608 \[gr-qc\]](#).
- [78] A. Placidi, S. Albanesi, A. Nagar, M. Orselli, S. Bernuzzi, and G. Grignani, Exploiting Newton-factorized, 2PN-accurate waveform multipoles in effective-one-body models for spin-aligned noncircularized binaries, *Phys. Rev. D* **105**, 104030 (2022), [arXiv:2112.05448 \[gr-qc\]](#).
- [79] A. Placidi, G. Grignani, T. Harmark, M. Orselli,

- S. Gliorio, and A. Nagar, 2.5PN accurate waveform information for generic-planar-orbit binaries in effective one-body models, *Phys. Rev. D* **108**, 024068 (2023), [arXiv:2305.14440 \[gr-qc\]](#).
- [80] A. Klein, Y. Boetzel, A. Gopakumar, P. Jetzer, and L. de Vittori, Fourier domain gravitational waveforms for precessing eccentric binaries, *Phys. Rev. D* **98**, 104043 (2018), [arXiv:1801.08542 \[gr-qc\]](#).
- [81] A. Klein, EFPE: Efficient fully precessing eccentric gravitational waveforms for binaries with long inspirals, (2021), [arXiv:2106.10291 \[gr-qc\]](#).
- [82] J. N. Arredondo, A. Klein, and N. Yunes, Efficient gravitational-wave model for fully-precessing and moderately eccentric, compact binary inspirals, *Phys. Rev. D* **110**, 044044 (2024), [arXiv:2402.06804 \[gr-qc\]](#).
- [83] G. Morras, G. Pratten, and P. Schmidt, Improved post-Newtonian waveform model for inspiralling precessing-eccentric compact binaries, *Phys. Rev. D* **111**, 084052 (2025), [arXiv:2502.03929 \[gr-qc\]](#).
- [84] G. Morras, Modeling gravitational wave modes from the inspiral of binaries with arbitrary eccentricity, *Phys. Rev. D* **112**, 084015 (2025), [arXiv:2507.00169 \[gr-qc\]](#).
- [85] I. Hinder, L. E. Kidder, and H. P. Pfeiffer, Eccentric binary black hole inspiral-merger-ringdown gravitational waveform model from numerical relativity and post-Newtonian theory, *Phys. Rev. D* **98**, 044015 (2018), [arXiv:1709.02007 \[gr-qc\]](#).
- [86] K. Paul, A. Maurya, Q. Henry, K. Sharma, P. Satheesh, Divyajyoti, P. Kumar, and C. K. Mishra, Eccentric, spinning, inspiral-merger-ringdown waveform model with higher modes for the detection and characterization of binary black holes, *Phys. Rev. D* **111**, 084074 (2025), [arXiv:2409.13866 \[gr-qc\]](#).
- [87] P. Manna, T. RoyChowdhury, and C. K. Mishra, Improved inspiral-merger-ringdown model for BBHs on elliptical orbits, *Phys. Rev. D* **111**, 124026 (2025), [arXiv:2409.10672 \[gr-qc\]](#).
- [88] A. Chattaraj, T. RoyChowdhury, Divyajyoti, C. K. Mishra, and A. Gupta, High accuracy post-Newtonian and numerical relativity comparisons involving higher modes for eccentric binary black holes and a dominant mode eccentric inspiral-merger-ringdown model, *Phys. Rev. D* **106**, 124008 (2022), [arXiv:2204.02377 \[gr-qc\]](#).
- [89] A. Buonanno and T. Damour, Effective one-body approach to general relativistic two-body dynamics, *Phys. Rev. D* **59**, 084006 (1999), [arXiv:gr-qc/9811091](#).
- [90] D. Bini and T. Damour, Gravitational radiation reaction along general orbits in the effective one-body formalism, *Phys. Rev. D* **86**, 124012 (2012), [arXiv:1210.2834 \[gr-qc\]](#).
- [91] T. Hinderer and S. Babak, Foundations of an effective-one-body model for coalescing binaries on eccentric orbits, *Phys. Rev. D* **96**, 104048 (2017), [arXiv:1707.08426 \[gr-qc\]](#).
- [92] Z. Cao and W.-B. Han, Waveform model for an eccentric binary black hole based on the effective-one-body-numerical-relativity formalism, *Phys. Rev. D* **96**, 044028 (2017), [arXiv:1708.00166 \[gr-qc\]](#).
- [93] X. Liu, Z. Cao, and Z.-H. Zhu, A higher-multipole gravitational waveform model for an eccentric binary black holes based on the effective-one-body-numerical-relativity formalism, *Class. Quant. Grav.* **39**, 035009 (2022), [arXiv:2102.08614 \[gr-qc\]](#).
- [94] X. Liu, Z. Cao, and L. Shao, Upgraded waveform model of eccentric binary black hole based on effective-one-body-numerical-relativity for spin-aligned binary black holes, *Int. J. Mod. Phys. D* **32**, 2350015 (2023), [arXiv:2306.15277 \[gr-qc\]](#).
- [95] D. Chiamarello and A. Nagar, Faithful analytical effective-one-body waveform model for spin-aligned, moderately eccentric, coalescing black hole binaries, *Phys. Rev. D* **101**, 101501 (2020), [arXiv:2001.11736 \[gr-qc\]](#).
- [96] A. Nagar, A. Bonino, and P. Retzegno, Effective one-body multipolar waveform model for spin-aligned, quasi-circular, eccentric, hyperbolic black hole binaries, *Phys. Rev. D* **103**, 104021 (2021), [arXiv:2101.08624 \[gr-qc\]](#).
- [97] A. Nagar and P. Retzegno, Next generation: Impact of high-order analytical information on effective one body waveform models for noncircularized, spin-aligned black hole binaries, *Phys. Rev. D* **104**, 104004 (2021), [arXiv:2108.02043 \[gr-qc\]](#).
- [98] A. Nagar, P. Retzegno, R. Gamba, S. Albanesi, A. Albertini, and S. Bernuzzi, Analytic systematics in next generation of effective-one-body gravitational waveform models for future observations, *Phys. Rev. D* **108**, 124018 (2023), [arXiv:2304.09662 \[gr-qc\]](#).
- [99] A. Ramos-Buades, A. Buonanno, M. Khalil, and S. Ossokine, Effective-one-body multipolar waveforms for eccentric binary black holes with nonprecessing spins, *Phys. Rev. D* **105**, 044035 (2022), [arXiv:2112.06952 \[gr-qc\]](#).
- [100] Y. Setyawati and F. Ohme, Adding eccentricity to quasi-circular binary-black-hole waveform models, *Phys. Rev. D* **103**, 124011 (2021), [arXiv:2101.11033 \[gr-qc\]](#).
- [101] M. d. L. Planas, A. Ramos-Buades, C. García-Quirós, H. Estellés, S. Husa, and M. Haney, Time-domain phenomenological multipolar waveforms for aligned-spin binary black holes in elliptical orbits, (2025), [arXiv:2503.13062 \[gr-qc\]](#).
- [102] T. Islam, Study of eccentric binary black hole mergers using numerical relativity and an inspiral-merger-ringdown model, (2024), [arXiv:2403.03487 \[gr-qc\]](#).
- [103] T. Islam, V. Varma, J. Lodman, S. E. Field, G. Khanna, M. A. Scheel, H. P. Pfeiffer, D. Gerosa, and L. E. Kidder, Eccentric binary black hole surrogate models for the gravitational waveform and remnant properties: comparable mass, nonspinning case, *Phys. Rev. D* **103**, 064022 (2021), [arXiv:2101.11798 \[gr-qc\]](#).
- [104] T. Islam, T. Venumadhav, A. K. Mehta, D. Wadekar, J. Roulet, I. Anantpurkar, J. Mushkin, B. Zackay, and M. Zaldarriaga, Data-driven extraction and phenomenology of eccentric harmonics in eccentric spinning binary black hole mergers, (2025), [arXiv:2509.20556 \[gr-qc\]](#).
- [105] P. J. Nee *et al.*, Eccentric binary black holes: A new framework for numerical relativity waveform surrogates, (2025), [arXiv:2510.00106 \[gr-qc\]](#).
- [106] A. Nagar, D. Chiamarello, R. Gamba, S. Albanesi, S. Bernuzzi, V. Fantini, M. Panzeri, and P. Retzegno, Effective-one-body waveform model for noncircularized, planar, coalescing black hole binaries. II. High accuracy by improving logarithmic terms in resummations, *Phys. Rev. D* **111**, 064050 (2025), [arXiv:2407.04762 \[gr-qc\]](#).
- [107] E. Thrane and C. Talbot, An introduction to bayesian inference in gravitational-wave astronomy: Parameter estimation, model selection, and hierarchical models,

- Publications of the Astronomical Society of Australia **36**, [10.1017/pasa.2019.2](https://doi.org/10.1017/pasa.2019.2) (2019).
- [108] G. Ashton and C. Talbot, Bilby-MCMC: an MCMC sampler for gravitational-wave inference, *Mon. Not. Roy. Astron. Soc.* **507**, 2037 (2021), [arXiv:2106.08730 \[gr-qc\]](https://arxiv.org/abs/2106.08730).
- [109] J. Veitch, V. Raymond, B. Farr, W. Farr, P. Graff, S. Vitale, B. Aylott, K. Blackburn, N. Christensen, M. Coughlin, W. Del Pozzo, F. Feroz, J. Gair, C.-J. Haster, V. Kalogera, T. Littenberg, I. Mandel, R. O’Shaughnessy, M. Pitkin, C. Rodriguez, C. Röver, T. Sidery, R. Smith, M. Van Der Sluys, A. Vecchio, W. Voudsen, and L. Wade, Parameter estimation for compact binaries with ground-based gravitational-wave observations using the lalinference software library, *Phys. Rev. D* **91**, 042003 (2015).
- [110] J. S. Speagle, Dynesty: a dynamic nested sampling package for estimating bayesian posteriors and evidences, *Monthly Notices of the Royal Astronomical Society* **493**, 3132 (2020).
- [111] F. Feroz, M. P. Hobson, E. Cameron, and A. N. Pettitt, Cpnest: a general-purpose bayesian inference tool using nested sampling, [arXiv:1306.2143 \[astro-ph.IM\]](https://arxiv.org/abs/1306.2143) (2013).
- [112] D. Foreman-Mackey, D. W. Hogg, D. Lang, and J. Goodman, emcee: The mcmc hammer, *Publications of the Astronomical Society of the Pacific* **125**, 306 (2013).
- [113] J. Buchner, A. Georgakakis, K. Nandra, L. Hsu, and et al., Pymultinest: a python interface for multinest, *Astronomy and Astrophysics* **564**, A125 (2014).
- [114] R. Abbott, T. D. Abbott, F. Acernese, K. Ackley, C. Adams, N. Adhikari, R. X. Adhikari, V. B. Adya, C. Affeldt, D. Agarwal, M. Agathos, *et al.*, GWTC-3: Compact Binary Coalescences Observed by LIGO and Virgo During the Second Part of the Third Observing Run, [arXiv e-prints](https://arxiv.org/abs/2111.03606), [arXiv:2111.03606](https://arxiv.org/abs/2111.03606) (2021), [arXiv:2111.03606 \[gr-qc\]](https://arxiv.org/abs/2111.03606).
- [115] J. S. Speagle, dynesty: a dynamic nested sampling package for estimating bayesian posteriors and evidences, *Monthly Notices of the Royal Astronomical Society* **493**, 3132–3158 (2020).
- [116] R. Abbott *et al.* (KAGRA, VIRGO, LIGO Scientific), Population of Merging Compact Binaries Inferred Using Gravitational Waves through GWTC-3, *Phys. Rev. X* **13**, 011048 (2023), [arXiv:2111.03634 \[astro-ph.HE\]](https://arxiv.org/abs/2111.03634).
- [117] J. Aasi *et al.* (LIGO Scientific), Advanced LIGO, *Class. Quant. Grav.* **32**, 074001 (2015), [arXiv:1411.4547 \[gr-qc\]](https://arxiv.org/abs/1411.4547).
- [118] P. Schmidt, M. Hannam, and S. Husa, Towards models of gravitational waveforms from generic binaries: A simple approximate mapping between precessing and non-precessing inspiral signals, *Phys. Rev. D* **86**, 104063 (2012), [arXiv:1207.3088 \[gr-qc\]](https://arxiv.org/abs/1207.3088).
- [119] P. Schmidt, F. Ohme, and M. Hannam, Towards models of gravitational waveforms from generic binaries II: Modelling precession effects with a single effective precession parameter, *Phys. Rev. D* **91**, 024043 (2015), [arXiv:1408.1810 \[gr-qc\]](https://arxiv.org/abs/1408.1810).
- [120] P. Ajith *et al.*, Inspiral-merger-ringdown waveforms for black-hole binaries with non-precessing spins, *Phys. Rev. Lett.* **106**, 241101 (2011), [arXiv:0909.2867 \[gr-qc\]](https://arxiv.org/abs/0909.2867).
- [121] L. Santamaria *et al.*, Matching post-Newtonian and numerical relativity waveforms: systematic errors and a new phenomenological model for non-precessing black hole binaries, *Phys. Rev. D* **82**, 064016 (2010), [arXiv:1005.3306 \[gr-qc\]](https://arxiv.org/abs/1005.3306).
- [122] G. Pratten, C. García-Quirós, M. Colleoni, A. Ramos-Buades, H. Estellés, M. Mateu-Lucena, R. Jaume, M. Haney, D. Keitel, J. E. Thompson, and S. Husa, Computationally efficient models for the dominant and subdominant harmonic modes of precessing binary black holes, *Phys. Rev. D* **103**, 104056 (2021).
- [123] M. Colleoni, F. A. Ramis Vidal, C. García-Quirós, S. Akçay, and S. Bera, Fast frequency-domain gravitational waveforms for precessing binaries with a new twist, *Phys. Rev. D* **111**, 104019 (2025).

Appendix A: Parameter estimation using the precessing IMRPhenomXPHM waveform model

This appendix presents tables summarizing the recovery of source parameters obtained using the precessing IMRPhenomXPHM waveform model for a set of eccentric signal injections with zero component spins and equal component masses. For each injection, parameter estimation is performed and the median values of the recovered parameters are reported, together with their associated 90% credible intervals. These results quantify the accuracy and robustness of the waveform model in recovering intrinsic and extrinsic source properties across different eccentricity configurations.

Appendix B: The χ_{eff} and χ_p recovery from precessing configuration :

This appendix presents posterior distributions of the effective inspiral spin parameter, χ_{eff} , and the effective precession spin parameter, χ_p , obtained from parameter estimation analyses using the precessing IMRPhenomXPHM waveform model. The results are shown as violin plots for injections with varying chirp masses \mathcal{M} and initial eccentricities. The shaded regions represent the full posterior distributions, while the coloured lines within each violin denote the corresponding 90% credible intervals. These figures illustrate the dependence of spin parameter recovery on the injected source properties and on the source's eccentricity.

Injection Parameters					Recovery Parameters						
M (M_{\odot})	\mathcal{M} (M_{\odot})	e (5 Hz)	e (10 Hz)	SNR	\mathcal{M} (M_{\odot})	m_1 (M_{\odot})	m_2 (M_{\odot})	D_L (Mpc)	χ_p	χ_{eff}	SNR
20	8.7	0.00	0.0000	27.9	$8.7^{+0.0}_{-0.0}$	$11.2^{+2.4}_{-1.1}$	$8.9^{+1.0}_{-1.4}$	$438.5^{+97.6}_{-103.1}$	$0.1^{+0.2}_{-0.1}$	$0.0^{+0.1}_{-0.0}$	$27.7^{+1.8}_{-1.8}$
30	13.1	0.00	0.0000	38.2	$13.0^{+0.0}_{-0.0}$	$16.6^{+2.7}_{-1.4}$	$13.5^{+1.2}_{-1.8}$	$448.6^{+74.7}_{-105.2}$	$0.1^{+0.2}_{-0.1}$	$0.0^{+0.0}_{-0.0}$	$38.0^{+1.8}_{-1.8}$
40	17.4	0.00	0.0000	48.0	$17.4^{+0.1}_{-0.1}$	$21.4^{+2.2}_{-1.3}$	$18.6^{+1.2}_{-1.7}$	$442.8^{+69.2}_{-103.7}$	$0.1^{+0.2}_{-0.1}$	$-0.0^{+0.0}_{-0.0}$	$47.8^{+1.9}_{-1.9}$
50	21.8	0.00	0.0000	56.8	$21.7^{+0.1}_{-0.1}$	$26.6^{+2.6}_{-1.5}$	$23.3^{+1.5}_{-2.0}$	$417.8^{+67.9}_{-82.9}$	$0.1^{+0.2}_{-0.1}$	$-0.0^{+0.0}_{-0.0}$	$56.6^{+1.9}_{-1.9}$
60	26.1	0.00	0.0000	65.1	$25.9^{+0.2}_{-0.2}$	$31.6^{+2.8}_{-1.6}$	$28.1^{+1.5}_{-2.3}$	$420.8^{+60.1}_{-78.8}$	$0.1^{+0.2}_{-0.1}$	$-0.0^{+0.0}_{-0.0}$	$65.0^{+1.9}_{-2.0}$
70	30.5	0.00	0.0000	73.1	$30.2^{+0.3}_{-0.3}$	$36.6^{+2.7}_{-1.7}$	$32.9^{+1.6}_{-2.4}$	$415.8^{+59.1}_{-74.7}$	$0.1^{+0.2}_{-0.1}$	$-0.0^{+0.0}_{-0.0}$	$73.0^{+1.9}_{-2.0}$
80	34.8	0.00	0.0000	80.8	$34.5^{+0.4}_{-0.4}$	$41.8^{+3.0}_{-2.0}$	$37.6^{+1.9}_{-2.8}$	$386.6^{+36.0}_{-75.0}$	$0.1^{+0.2}_{-0.1}$	$-0.0^{+0.0}_{-0.0}$	$80.7^{+1.8}_{-1.8}$
20	8.7	0.10	0.0479	27.9	$8.7^{+0.0}_{-0.0}$	$11.1^{+2.2}_{-1.0}$	$9.0^{+0.9}_{-1.4}$	$452.7^{+89.5}_{-119.5}$	$0.1^{+0.2}_{-0.1}$	$0.0^{+0.1}_{-0.0}$	$27.6^{+1.8}_{-1.8}$
30	13.1	0.10	0.0475	38.3	$13.1^{+0.0}_{-0.0}$	$16.7^{+2.6}_{-1.6}$	$13.5^{+1.3}_{-1.7}$	$450.6^{+76.5}_{-95.4}$	$0.1^{+0.2}_{-0.1}$	$0.0^{+0.0}_{-0.0}$	$38.0^{+1.8}_{-1.8}$
40	17.4	0.10	0.0472	48.0	$17.4^{+0.1}_{-0.1}$	$21.5^{+2.2}_{-1.4}$	$18.6^{+1.2}_{-1.7}$	$437.4^{+66.9}_{-94.9}$	$0.1^{+0.2}_{-0.1}$	$-0.0^{+0.0}_{-0.0}$	$47.8^{+1.8}_{-1.8}$
50	21.8	0.10	0.0468	56.8	$21.7^{+0.1}_{-0.1}$	$26.4^{+2.4}_{-1.3}$	$23.5^{+1.2}_{-1.9}$	$430.8^{+64.3}_{-77.8}$	$0.1^{+0.2}_{-0.1}$	$-0.0^{+0.0}_{-0.0}$	$56.5^{+1.9}_{-1.8}$
60	26.1	0.10	0.0465	65.1	$25.9^{+0.2}_{-0.2}$	$31.3^{+2.6}_{-1.4}$	$28.3^{+1.3}_{-2.1}$	$427.2^{+59.6}_{-77.1}$	$0.1^{+0.2}_{-0.1}$	$-0.0^{+0.0}_{-0.0}$	$64.8^{+1.9}_{-1.9}$
70	30.5	0.10	0.0461	73.3	$30.4^{+0.3}_{-0.3}$	$36.8^{+2.8}_{-1.7}$	$33.2^{+1.6}_{-2.5}$	$421.1^{+59.4}_{-71.1}$	$0.1^{+0.2}_{-0.1}$	$-0.0^{+0.0}_{-0.0}$	$73.1^{+2.1}_{-2.0}$
80	34.8	0.10	0.0458	80.9	$34.6^{+0.4}_{-0.4}$	$41.9^{+3.1}_{-1.9}$	$37.8^{+1.8}_{-2.9}$	$383.0^{+32.7}_{-70.2}$	$0.1^{+0.2}_{-0.1}$	$-0.0^{+0.0}_{-0.0}$	$80.7^{+1.7}_{-1.7}$
20	8.7	0.20	0.0999	27.9	$8.7^{+0.0}_{-0.0}$	$11.4^{+2.7}_{-1.2}$	$8.9^{+1.0}_{-1.5}$	$471.9^{+76.3}_{-118.2}$	$0.2^{+0.3}_{-0.1}$	$0.0^{+0.1}_{-0.0}$	$27.6^{+1.8}_{-1.8}$
30	13.1	0.20	0.0991	38.3	$13.1^{+0.0}_{-0.0}$	$16.2^{+2.8}_{-1.1}$	$14.0^{+1.0}_{-2.0}$	$456.9^{+73.7}_{-101.4}$	$0.1^{+0.2}_{-0.1}$	$0.0^{+0.0}_{-0.0}$	$37.9^{+1.8}_{-1.7}$
40	17.4	0.20	0.0984	48.1	$17.4^{+0.1}_{-0.1}$	$21.4^{+2.2}_{-1.3}$	$18.7^{+1.2}_{-1.7}$	$429.5^{+75.8}_{-88.8}$	$0.1^{+0.2}_{-0.1}$	$-0.0^{+0.0}_{-0.0}$	$47.7^{+1.9}_{-1.9}$
50	21.8	0.20	0.0977	56.9	$21.7^{+0.1}_{-0.1}$	$26.3^{+2.2}_{-1.3}$	$23.5^{+1.2}_{-1.8}$	$420.5^{+68.1}_{-77.7}$	$0.1^{+0.2}_{-0.1}$	$-0.0^{+0.0}_{-0.0}$	$56.4^{+1.9}_{-1.8}$
60	26.1	0.20	0.0969	65.3	$26.2^{+0.2}_{-0.2}$	$31.4^{+2.6}_{-1.6}$	$28.8^{+1.2}_{-2.2}$	$415.1^{+70.8}_{-75.1}$	$0.1^{+0.2}_{-0.1}$	$0.0^{+0.0}_{-0.0}$	$64.8^{+1.9}_{-1.9}$
70	30.5	0.20	0.0962	73.2	$29.9^{+0.3}_{-0.3}$	$36.7^{+2.8}_{-2.0}$	$32.3^{+1.9}_{-2.4}$	$418.1^{+50.3}_{-60.2}$	$0.2^{+0.2}_{-0.1}$	$-0.1^{+0.0}_{-0.0}$	$72.7^{+1.8}_{-1.9}$
80	34.8	0.20	0.0955	80.9	$34.1^{+0.4}_{-0.4}$	$41.1^{+2.8}_{-1.8}$	$37.3^{+1.7}_{-2.6}$	$389.1^{+35.9}_{-68.8}$	$0.1^{+0.2}_{-0.1}$	$-0.1^{+0.0}_{-0.0}$	$80.3^{+1.8}_{-1.8}$
20	8.7	0.30	0.1599	28.0	$8.8^{+0.0}_{-0.0}$	$11.9^{+2.7}_{-1.6}$	$8.6^{+1.3}_{-1.4}$	$459.5^{+92.1}_{-107.5}$	$0.2^{+0.2}_{-0.1}$	$0.1^{+0.1}_{-0.0}$	$27.3^{+1.7}_{-1.8}$
30	13.1	0.30	0.1588	38.4	$13.2^{+0.0}_{-0.0}$	$16.6^{+2.7}_{-1.3}$	$13.9^{+1.1}_{-1.9}$	$466.4^{+70.2}_{-85.1}$	$0.2^{+0.2}_{-0.1}$	$0.0^{+0.0}_{-0.0}$	$37.7^{+1.6}_{-1.8}$
40	17.4	0.30	0.1577	48.3	$17.5^{+0.1}_{-0.1}$	$21.3^{+2.2}_{-1.1}$	$19.0^{+1.0}_{-1.7}$	$433.0^{+75.5}_{-88.1}$	$0.1^{+0.2}_{-0.1}$	$-0.0^{+0.0}_{-0.0}$	$47.4^{+1.8}_{-1.9}$
50	21.8	0.30	0.1566	57.1	$21.9^{+0.1}_{-0.1}$	$26.3^{+2.0}_{-1.0}$	$24.1^{+0.9}_{-1.7}$	$441.9^{+65.7}_{-97.0}$	$0.1^{+0.2}_{-0.1}$	$0.0^{+0.0}_{-0.0}$	$56.0^{+1.8}_{-1.9}$
60	26.1	0.30	0.1555	65.7	$26.0^{+0.2}_{-0.2}$	$31.7^{+2.8}_{-1.5}$	$28.3^{+1.4}_{-2.3}$	$444.0^{+54.3}_{-70.0}$	$0.2^{+0.2}_{-0.1}$	$-0.0^{+0.0}_{-0.0}$	$64.5^{+1.9}_{-1.8}$
70	30.5	0.30	0.1545	73.3	$29.9^{+0.3}_{-0.3}$	$36.0^{+2.6}_{-1.4}$	$32.9^{+1.4}_{-2.3}$	$412.1^{+58.9}_{-84.9}$	$0.2^{+0.2}_{-0.1}$	$-0.1^{+0.0}_{-0.0}$	$71.9^{+1.9}_{-1.9}$
80	34.8	0.30	0.1534	81.6	$35.4^{+0.4}_{-0.4}$	$42.0^{+0.9}_{-0.8}$	$39.4^{+0.6}_{-0.7}$	$430.1^{+26.9}_{-42.5}$	$0.5^{+0.1}_{-0.3}$	$0.0^{+0.0}_{-0.0}$	$80.2^{+1.6}_{-1.7}$
20	8.7	0.40	0.2321	28.1	$8.9^{+0.0}_{-0.0}$	$12.0^{+2.8}_{-1.2}$	$8.8^{+0.9}_{-1.5}$	$505.0^{+66.6}_{-98.0}$	$0.5^{+0.3}_{-0.3}$	$0.1^{+0.1}_{-0.0}$	$26.8^{+1.5}_{-1.6}$
30	13.1	0.40	0.2306	38.8	$13.4^{+0.1}_{-0.0}$	$16.7^{+2.9}_{-1.2}$	$14.2^{+1.0}_{-2.0}$	$485.1^{+79.6}_{-92.3}$	$0.2^{+0.4}_{-0.1}$	$0.1^{+0.0}_{-0.0}$	$37.2^{+1.8}_{-1.7}$
40	17.4	0.40	0.2291	48.6	$17.8^{+0.1}_{-0.1}$	$21.8^{+2.4}_{-1.1}$	$19.3^{+1.1}_{-1.8}$	$479.4^{+68.9}_{-87.0}$	$0.2^{+0.2}_{-0.1}$	$0.1^{+0.0}_{-0.0}$	$46.8^{+1.7}_{-1.8}$
50	21.8	0.40	0.2276	57.5	$22.2^{+0.1}_{-0.1}$	$26.8^{+2.2}_{-1.2}$	$24.2^{+1.1}_{-1.8}$	$439.2^{+75.4}_{-91.7}$	$0.1^{+0.2}_{-0.1}$	$0.0^{+0.0}_{-0.0}$	$55.4^{+1.9}_{-1.9}$
60	26.1	0.40	0.2262	65.6	$26.2^{+0.2}_{-0.2}$	$31.6^{+0.7}_{-0.7}$	$28.7^{+0.6}_{-0.5}$	$470.1^{+38.6}_{-41.9}$	$0.7^{+0.1}_{-0.2}$	$-0.0^{+0.0}_{-0.0}$	$63.0^{+1.7}_{-1.6}$
70	30.5	0.40	0.2248	73.9	$30.5^{+0.4}_{-0.4}$	$36.5^{+0.7}_{-0.7}$	$33.5^{+0.6}_{-0.6}$	$446.3^{+34.1}_{-43.4}$	$0.5^{+0.1}_{-0.1}$	$-0.0^{+0.0}_{-0.0}$	$71.2^{+1.7}_{-1.6}$
80	34.8	0.40	0.2234	81.9	$34.0^{+0.8}_{-0.6}$	$41.5^{+0.9}_{-0.6}$	$36.8^{+1.2}_{-0.9}$	$380.0^{+37.6}_{-37.9}$	$0.9^{+0.1}_{-0.2}$	$-0.2^{+0.1}_{-0.1}$	$79.0^{+1.7}_{-1.7}$
20	8.7	0.50	0.3204	28.4	$9.1^{+0.0}_{-0.0}$	$13.4^{+0.8}_{-1.1}$	$8.3^{+0.7}_{-0.4}$	$493.9^{+106.8}_{-109.1}$	$0.6^{+0.4}_{-0.1}$	$0.2^{+0.0}_{-0.0}$	$25.3^{+1.6}_{-1.6}$
30	13.1	0.50	0.3185	39.3	$13.8^{+0.1}_{-0.1}$	$18.0^{+1.9}_{-0.8}$	$14.0^{+0.6}_{-1.2}$	$560.8^{+50.1}_{-58.8}$	$0.7^{+0.1}_{-0.1}$	$0.2^{+0.0}_{-0.0}$	$36.2^{+1.6}_{-1.5}$
40	17.4	0.50	0.3167	49.5	$18.5^{+0.1}_{-0.1}$	$22.6^{+1.7}_{-1.2}$	$20.0^{+1.1}_{-1.4}$	$485.9^{+78.3}_{-102.1}$	$0.3^{+0.2}_{-0.2}$	$0.1^{+0.0}_{-0.0}$	$45.5^{+1.7}_{-1.7}$
50	21.8	0.50	0.3149	58.7	$23.2^{+0.2}_{-0.2}$	$27.7^{+1.3}_{-0.7}$	$25.6^{+0.7}_{-0.7}$	$490.8^{+69.3}_{-89.1}$	$0.6^{+0.2}_{-0.4}$	$0.1^{+0.0}_{-0.0}$	$54.0^{+1.8}_{-1.7}$
60	26.1	0.50	0.3131	66.8	$27.4^{+0.3}_{-0.3}$	$34.1^{+0.6}_{-0.6}$	$29.1^{+0.5}_{-0.4}$	$447.7^{+70.0}_{-64.9}$	$0.8^{+0.1}_{-0.1}$	$0.1^{+0.0}_{-0.0}$	$61.2^{+2.0}_{-2.0}$
70	30.5	0.50	0.3113	76.4	$32.3^{+0.4}_{-0.4}$	$39.6^{+0.6}_{-0.6}$	$34.9^{+0.4}_{-0.4}$	$416.5^{+62.8}_{-59.0}$	$0.8^{+0.1}_{-0.1}$	$-0.0^{+0.0}_{-0.0}$	$70.6^{+2.1}_{-2.0}$
80	34.8	0.50	0.3096	84.1	$34.7^{+0.9}_{-0.8}$	$55.9^{+2.4}_{-2.6}$	$29.1^{+1.3}_{-1.5}$	$352.2^{+34.7}_{-32.8}$	$1.0^{+0.0}_{-0.0}$	$-0.2^{+0.1}_{-0.1}$	$77.5^{+1.8}_{-1.7}$

TABLE II: Recovery of parameters using a precessing IMRPhenomXPHM waveform model for various eccentric injections with zero spin and equal component masses. Median value of recovered parameters quoted along with the 90% credible levels.

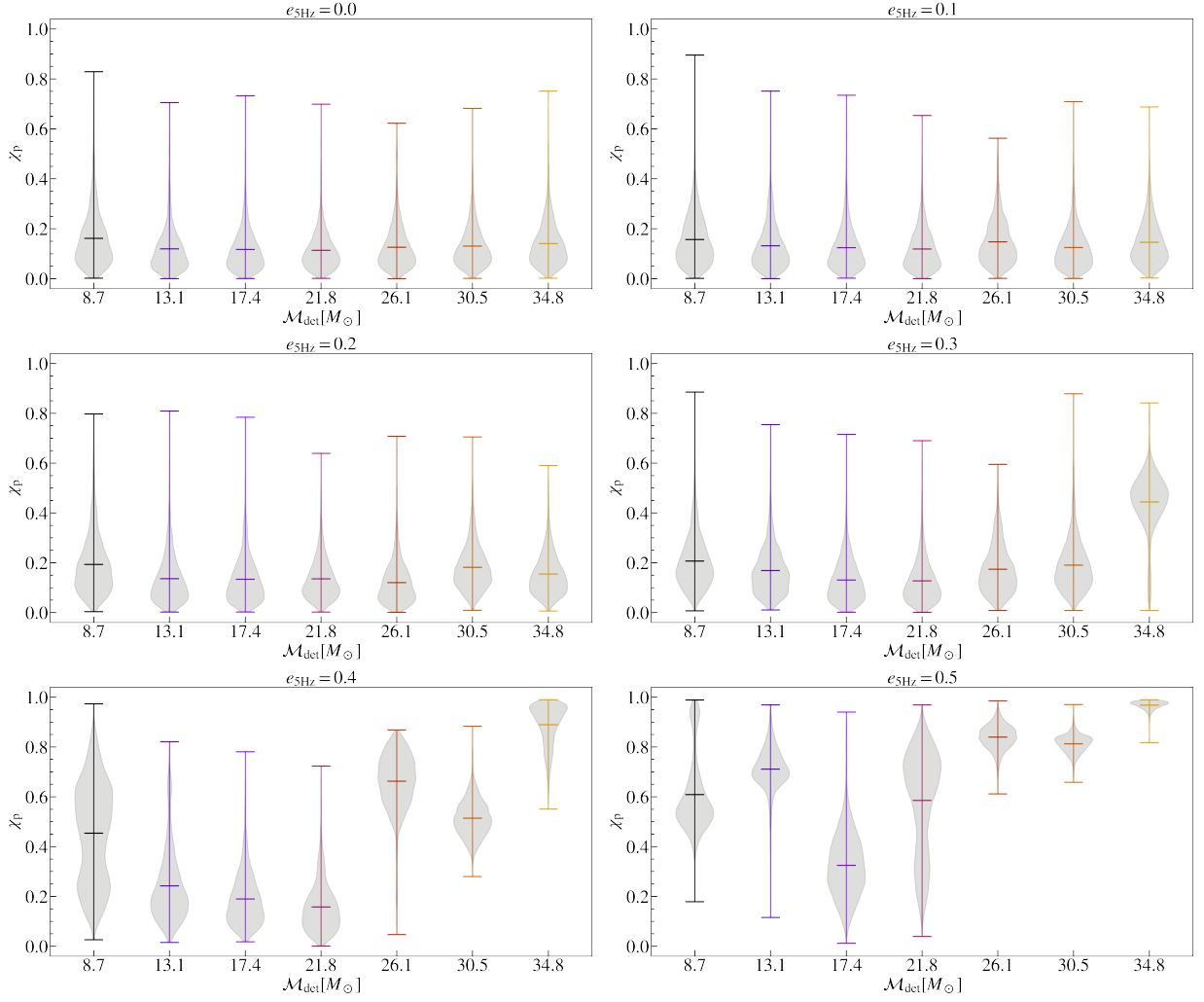


FIG. 10: The χ_p posterior violin plots for varying injected \mathcal{M} and initial eccentricities. The colored lines inside the shaded posteriors indicate 90% credible interval. Posterior distributions largely support zero precessing spins for all cases except for $e \geq 0.4$.

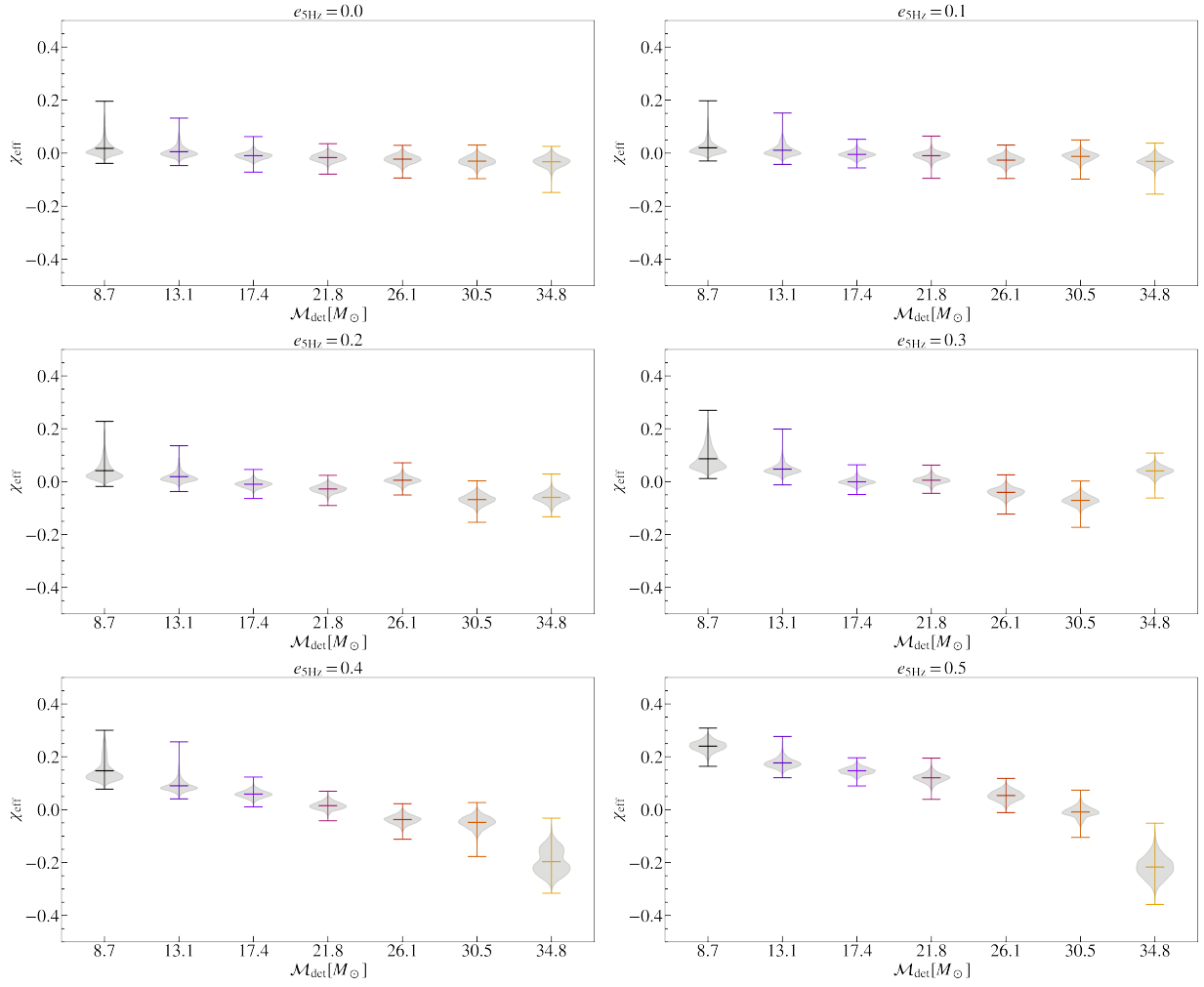


FIG. 11: The χ_{eff} posterior violin plots for varying injected \mathcal{M} and initial eccentricities. The colored lines inside the shaded posteriors indicate 90% credible interval. Posterior distributions show zero effective spins for all cases except for $e \geq 0.4$ where there are deviations from zero.